Computers and Fluids 259 (2023) 105899

Contents lists available at ScienceDirect

Computers and Fluids

journal homepage: www.elsevier.com/locate/compfluid

A unified consistent source term computational algorithm for the γ-based compressible multi-fluid flow model

Li Ge [a], Li Libin [a], Liu Qingquan [a], Feng Chun [b], Wang Xiaoliang [a,*]

[a] Department of Mechanics, School of Aerospace Engineering, Beijing Institute of Technology, Beijing 100081, China
[b] Institute of Mechanics, Chinese Academy of Sciences, Beijing 100190, China

ARTICLE INFO

Keywords:
Compressible multi-fluid flow
Consistent algorithm
One-fluid preservation
Moving interface
Interface sharpening

ABSTRACT

Using the criterion of one-fluid preservation, we developed a consistent algorithm for the source term to solve the γ-based compressible multi-fluid flow model with three approximate Riemann solvers, namely the Lax–Friedrichs (LxF), Kurganov, and Harten–Lax–van Leer contact (HLLC) solvers. The consistent algorithm comprises a standard Godunov solver with a high-order reconstruction and a consistent source term integration part. We prove that the present algorithm is consistent with Abgrall's criterion of the moving-material-interface property in the finite volume method framework. The cell boundary velocity for the source term discretization is found to be the same as HLLC solvers from five-equation model, but for the first time for LxF and Kurganov Riemann solvers. We develop 12 compressible multi-fluid solvers by combining four reconstruction schemes and three approximate Riemann solvers together with their consistent-source-term integration algorithms. All 12 solvers can maintain the one-fluid preservation and moving-material-interface properties numerically in several one- and two-dimensional example cases. The simulation of an underwater explosion demonstrates that a boundary-variation-diminishing reconstruction predicts an interface with width controlled within approximately three cells which is independent of the Riemann solver. The simulation of an explosion near a free surface demonstrates that the proposed model can simulate a severe compressible multi-fluid flow involving an interface across which there are large differences in density, pressure and parameters in the equation of state. In conclusion, the proposed consistent algorithm provides a unified framework for one kind of non-conservative hyperbolic system into a conservative hyperbolic system and a source term with velocity divergence, where the former can be computed by classical Godunov-type algorithms and the latter can be solved by the proposed consistent algorithm.

1. Introduction

Compressible multi-fluid flow has recently attracted much interest for its value in a wide range of engineering problems, such as underwater explosions [26], droplet and bubble dynamics and their interaction with shock waves in combustion system and high-speed flows [16], and the breakage of kidney stones by burst waves in medical engineering [17]. Furthermore, the addition of an interface makes the numerical computation more difficult than that of compressible single-fluid flow; e.g., in the capture of an interface, the simulation of the interaction of an interface with shock waves, and solving interface problems with very large differences in physical parameters such as density and pressure across the interface [23,25].

The cornerstone to the study of multi-fluid or multiphase compressibility is the seven-equation model developed in 1986 by Baer and Nunziato [5], which was initially proposed for reactive multiphase flow and then used for other compressible multi-fluid flows. Later, Kapila [18] derived a five-equation model through the asymptotic reduction of the seven-equation model under stiff mechanical relaxation, where a single velocity and a single pressure is shared by different phases. Another five-equation model similar to that of Kapila [18] was proposed by Allaire et al. [3] for compressible multi-fluid flow problems without reactions. The above models can be easily closed using nonlinear equations of state (EOSs), such as the stiffened gas (SG) EOS, Jones–Wilkins–Lee EOS, and Cochran–Chan EOS, which can handle problems involving a complex medium. In the case that the EOS is simple and has a limited number of parameters, the well-known γ-based model, which is based on the mixture rules and was first proposed by

---

* Corresponding author.
E-mail address: wangxiaoliang52086@126.com (W. Xiaoliang).

https://doi.org/10.1016/j.compfluid.2023.105899
Received 1 September 2022; Received in revised form 30 March 2023; Accepted 16 April 2023

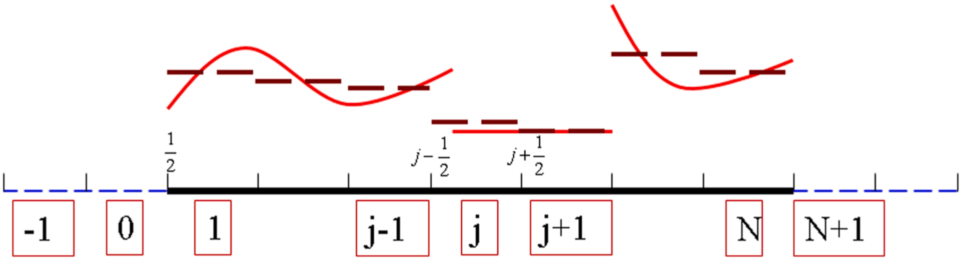

Fig. 1. Mesh system in one dimension for the FVM, where the computational domain is subdivided into N cells with indices 1 to N and ghost cells are used for boundary treatment. The red solid lines show the real field variable distribution and the dashed lines the volume-averaged value for each cell.

Abgrall [1] for perfect gases and later used for SG fluids by Shyue [28], has been widely used. Refer to a recent review by Maltsev et al. [23] for details of the theoretical advances in compressible multi-fluid flow and extensions.

The computations of the above compressible multi-fluid flow models are more difficult than those of a single-phase compressible fluid flow model. There are several numerical frameworks for computing compressible fluid flows with interfaces, such as the front tracking method [11], the level set method [4], and the ghost fluid method [8], but we are here concerned with the recently developed diffused-interface method (DIM) within the finite volume method (FVM) where the interface of two fluids is modeled as a mixed fluid on several meshes. The computational difficulty lies in the above model being a non-conservational hyperbolic system that involves several structures that must be preserved by the numerical model.

Abgrall and his collaborators assumed in a series of studies [2,24] that “any physical contact discontinuity should remain a contact discontinuity.” On this basis, they handled the conservation part (i.e., the Euler equation) using a Godunov algorithm and separately handled the non-conservation part for the function of the specific heat ratio $(1/(\gamma-1))$, and they derived algorithms for different Riemann solvers, including the Rusonav solver, the Harten–Lax–van Leer solver, and the Roe solver, for the γ-based model. The γ-based model was extended by Shyue to fluids with the SG EOS [28], the van der Waals EOS [29], and the Mie–Gruneisen EOS [30]. In contrast with Abgrall, Shyue [28–30] developed a numerical algorithm directly for the whole model in a non-conservation form within the framework of the wave propagation method using the Roe approximate Riemann solver. Allaire et al. [3] developed the five-equation model as a conservation model with a source term involving velocity divergence. They directly used a Godunov scheme with the Roe approximate Riemann solver for the numerical flux computation, and they directly proposed a cell boundary velocity by averaging the left and right numerical interpolations of velocity without justification, simply conducting a numerical examination of the pure-material traveling problem. This framework of writing the five-equation model with a left-side conservation term and a right-side source term including velocity divergence was extended by Johnsen and Colonius [17] and Wang et al. [35] for several multiphase compressible flow problems, where they used the Harten–Lax–van Leer contact (HLLC) Riemann solver with complex treatment of the velocity divergence term. The above numerical schemes lie within the framework of the FVM. He et al. [13] recently proposed a consistent algorithm for the γ-based model within the framework of the finite difference method (FDM) in the form of a conservation law with a velocity-divergence source term by claiming a new criterion that “a multicomponent-fluid algorithm should have the ability of maintaining a pure single-fluid.”

The DIM for compressible flow often suffers the problem of large dissipation that widens the interface, which can lead to an incorrect computation even with consistent treatment of the source term. Therefore, in the last decade, several contributions to the literature have narrowed the numerical interface, which is often called the interface sharpening technique, adopting the anti-diffusion method [32], interface compression method [26], incremental-stencil weight-essential-non-oscillation (WENO) method [35], and target-WENO method [9]. The recently developed interface sharpening technique in the DIM adopting the THINC (Tangent of Hyperbola for Interface Capturing) method for cell reconstruction [7,31,33] exhibits good ability in modeling compressible multi-fluid flow problems. More importantly, the technique can be easily extended to an unstructured mesh without losing numerical stability in the interface sharpening and the interaction with complex shock waves.

The above review of the literature mentioned many achievements in modeling and computing the compressible multi-fluid flow problem. However, it seems that there is still no unified treatment of the γ-based non-conservation model for different kinds of Riemann solvers for compressible multi-fluid flows. The consistent treatment of the velocity-divergence term differs from the use of different approximate Riemann solvers. He et al. [13] claimed that Abgrall’s criterion does not yield a consistent discretization form of the velocity-divergence source term in the FDM. Can the two criterions of He et al. [13] and Abgrall [2,24] result in an equivalent numerical consistent algorithm in the FVM?

To answer the above question, we developed a unified consistent algorithm of the γ-based model for three different approximate Riemann solvers in this paper. The remainder of the paper is arranged as follows. Section 2 introduces the mathematical model and the numerical discretization. Section 3 develops a consistent treatment of the velocity-divergence source term for three widely used approximate Riemann solvers. Section 4 shows that the present consistent treatment is consistent with Abgrall’s criterion. Section 5 computes several one-dimensional (1D) and two-dimensional (2D) compressible multi-fluid problems to demonstrate the abilities of the proposed consistent algorithms. Finally, conclusions are presented in Section 6.

2. Mathematical model and numerical discretization

2.1. Mathematical model

There are several formulations of the compressible multi-fluid flow problem, such as five-equation model [3] and γ-based model [28], as recently summarized in [23]. Here, to illustrate a new consistent algorithm for the phase interface solution in multi-fluid flow, we choose the γ-based model as expressed in Eq. (1) in 1D form in the form with a left conservation part and a right velocity-divergence term. The closure of EOS used in this study is the stiffened gas model as expressed in Eq. (2).

$$\frac{\partial}{\partial t}\begin{pmatrix}\rho\\ \rho u\\ E\\ \dfrac{1}{\gamma-1}\\ \dfrac{\gamma p_\infty}{\gamma-1}\end{pmatrix}+\frac{\partial}{\partial x}\begin{pmatrix}\rho u\\ \rho u^2+p\\ u(E+p)\\ \dfrac{u}{\gamma-1}\\ \dfrac{u\gamma p_\infty}{\gamma-1}\end{pmatrix}=\begin{pmatrix}0\\ 0\\ 0\\ \dfrac{1}{\gamma-1}\dfrac{\partial u}{\partial x}\\ \dfrac{\gamma p_\infty}{\gamma-1}\dfrac{\partial u}{\partial x}\end{pmatrix} \tag{1}$$

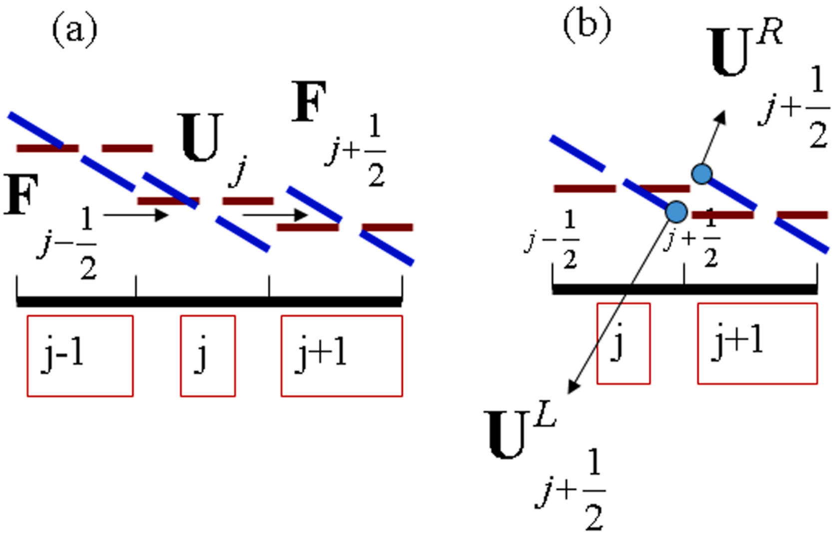

Fig. 2. Stencils used for cell j (a) and the left and right reconstructed variables $\mathbf{U}^L_{j+\frac{1}{2}}$, $\mathbf{U}^R_{j+\frac{1}{2}}$ for the boundary between cells j and $j+1$ (b).

$$\rho e = \frac{p + \gamma p_\infty}{\gamma - 1} \tag{2}$$

Here, ρ, u, and p are, respectively the density, velocity, and pressure and $E = \rho\left(\frac{1}{2}u^2 + e\right)$ is the total energy. In the closure equation, γ is the ratio of specific heat, and p_∞ is a prescribed pressure-like constant.

The γ-based model in Eq. (1) describes a wide class of compressible multi-fluid problems, such as underwater explosions [28], and two-phase problems with different ratios of specific heat, such as an interaction between a shock wave and gas bubble [12].

2.2. Semi-discrete formulation

As shown in Fig. 1, we adopt the FVM to discretize Eq. (1). First, Eq. (1) is rewritten as in Eq. (3) in the conservation form with the conservative term **U**, flux term **F**, and the source term **S**.

$$\mathbf{U}_t + \mathbf{F}_x = \mathbf{S} \tag{3}$$

Here, the conservative term, the flux term, and the source term are, respectively$\mathbf{U} = \begin{pmatrix}\rho & \rho u & E & 1/(\gamma-1) & \gamma p_\infty/(\gamma-1)\end{pmatrix}^T$, $\mathbf{F} = \begin{pmatrix}\rho u & \rho u^2 + p & u(E+p) & u/(\gamma-1) & u\gamma p_\infty/(\gamma-1)\end{pmatrix}^T$, and $\mathbf{S} = \begin{pmatrix}0 & 0 & 0 & \frac{1}{\gamma-1}u_x & \frac{\gamma p_\infty}{\gamma-1}u_x\end{pmatrix}^T$.

For cell j in Fig. 1, the average value of the conservative variable is defined as $\overline{\mathbf{U}}_j = \frac{1}{\Delta x}\int_{x_{j-\frac{1}{2}}}^{x_{j+\frac{1}{2}}} \mathbf{U}(x,t)dx$. By integrating over cell j, we obtain the semi-discrete formulation of Eq. (1) as written in Eq. (4), noting that the averaging symbol "-" is omitted in the semi-discrete formulation.

$$\frac{d}{dt}\mathbf{U}_j = -\frac{1}{\Delta x}\left[\mathbf{F}_{j+\frac{1}{2}} - \mathbf{F}_{j-\frac{1}{2}}\right] + \frac{1}{\Delta x}\int_{x_{j-\frac{1}{2}}}^{x_{j+\frac{1}{2}}} \mathbf{S}dx \tag{4}$$

Here, the integrated source term is $\frac{1}{\Delta x}\int_{x_{j-\frac{1}{2}}}^{x_{j+\frac{1}{2}}} \mathbf{S}dx = \frac{1}{\Delta x}\begin{pmatrix} 0 \\ 0 \\ 0 \\ \frac{1}{\gamma_j - 1}\left(\widehat{u}_{j+\frac{1}{2}} - \widehat{u}_{j-\frac{1}{2}}\right) \\ \frac{\gamma_j p_{\infty j}}{\gamma_j - 1}\left(\widehat{u}_{j+\frac{1}{2}} - \widehat{u}_{j-\frac{1}{2}}\right) \end{pmatrix}$ and the numerical flux term is $\mathbf{F}_{j+\frac{1}{2}} = \mathbf{F}_{j+\frac{1}{2}}\left(\mathbf{U}^L_{j+\frac{1}{2}}, \mathbf{U}^R_{j+\frac{1}{2}}\right)$, where $\mathbf{U}^L_{j+\frac{1}{2}}$ and $\mathbf{U}^R_{j+\frac{1}{2}}$ are reconstructed variables at the boundary between cells j and $j+1$, as shown in Fig. 2. $\widehat{u}_{j+\frac{1}{2}}$ and $\widehat{u}_{j-\frac{1}{2}}$ are cell boundary velocities on the right and left side of cell j for the source term integration. The left side of Eq. (1) is hyperbolic (see Appendix A for proof). The computation of the numerical flux $\mathbf{F}_{j+\frac{1}{2}} = \mathbf{F}_{j+\frac{1}{2}}\left(\mathbf{U}^L_{j+\frac{1}{2}}, \mathbf{U}^R_{j+\frac{1}{2}}\right)$ can be computed by the standard computation using approximate Riemann solvers [34]. However, the numerical computation of the integrated source term is difficult in that at least two requirements must be satisfied. First, the discrete form must satisfy the pure fluid transformation condition, which is to say that two contacting materials moving with the same velocity under a zero pressure gradient must maintain their form as two contacting moving materials. Second, the discrete form must revert to one-phase fluid flow if the two phases are of the same material. We develop a consistent algorithm satisfying the above two requirements.

2.3. Spatial reconstruction

Before developing the new unified algorithm for the source term, the high-order schemes used in this study are presented. As shown in Fig. 2, a stencil of three cells or five cells in Fig. 2(a) is used to reconstruct the cell boundary values in Fig. 2(b). The reconstruction must prevent numerical oscillation due to dispersion error. In this study, the classical MUSCL method using polynomial interpolation [34], THINC method using the hyperbolic tangent function [37], and classical WENO proposed by Jiang and Shu [15] are chosen for reconstruction of left and right values at a cell boundary. Additionally, the boundary variation diminishing (BVD) method [33] is used to sharpen the diffusing interface as another reconstruction method with two kinds of reconstruction methods which can be the schemes mentioned above or other high-order reconstruction schemes. Conservative, primitive, and characteristic variables can be used for variable reconstruction. In this study, the primitive variable of $(\rho, u, p, \gamma, p_\infty)^T$ is used for reconstruction. The parameter β controlling the numerical diffusion in the THINC method takes a value of 1.15 [33]. In the BVD method [33], β takes a value of 1.15 for shock capture which reflects a similar behavior of 2nd order of MUSCL scheme and a value of 1.6 for interface sharpening aim, respectively.

2.4. *Temporal integration and the multidimensional case*

We use a two-step Runge–Kutta method for temporal integration in numerical examples using MUSCL, THINC and BVD reconstruction schemes, and we use a three-stage third-order integration method for the WENO reconstruction scheme [33,34].

We simply take a dimension-by-dimension approach to extend the above 1D algorithm to the multidimensional case. For example, in the 2D case, a uniform Cartesian mesh that is fixed in x and y directions is used, reconstructions along these two directions are then implemented sequentially for the numerical calculation of fluxes, together with the consistent treatment of the source term presented in Section 3, and a temporal integration is finally executed.

3. Consistent treatment of the source term for different Riemann solvers

The first three equations in the semi-discrete Eq. (4) are the same as those for the compressible Euler equations. The source term in the fourth and fifth equations of Eq. (4) should be carefully treated to satisfy the two requirements presented in Section 2.2. Saurel and Abgrall [1999] proposed a discrete formulation in non-conservative form for several approximate Riemann solvers with the criterion that "the velocity and pressure equilibria should be maintained during time updates" [1]. He et al. [13] developed a criterion for the multi-fluid compressible flow in the FDM, where they stated that "A multi-fluid algorithm should have the ability of maintaining a pure single-fluid." They also stated that no consistent term can be obtained using Abgrall's criterion [1] in the FDM of the multi-fluid compressible flow. We refer to the criterion of He et al. [13] as the "single-fluid preservation criterion" and the criterion of Saurel and Abgrall's [1996] as the "moving-material-interface preservation criterion."

We here directly deal with the above problem in the unified framework of Eq. (1), which is written in the form of a conservation law on the left side and another velocity-divergence source term on the right side. In this way, we use the Riemann solver theory easily both numerically and practically for the left side of Eq. (1), and only the consistent treatment of the right side involving a velocity divergence term need be carefully handled. We apply the single-fluid preservation criterion of He et al. [13], originally adopted for the FDM, to the FVM formulation in this study, and we later prove that the algorithm derived using the single-fluid preservation criterion has the pure moving-material-interface property. Using a first-order Euler integration for the time marching term, the fourth and fifth equations of the semi-discrete scheme are written as Eqs. (5) and (6), where $F^{(k)}_{j+\frac{1}{2}}$ means the kth term of the flux vector $\mathbf{F}_{j+\frac{1}{2}}$.

$$\left(\frac{1}{\gamma-1}\right)_j^{n+1}=\left(\frac{1}{\gamma-1}\right)_j^{n}-\frac{\Delta t}{\Delta x}\left(F^{(4)}_{j+\frac{1}{2}}-F^{(4)}_{j-\frac{1}{2}}\right)+\frac{\Delta t}{\Delta x}\left(\frac{1}{\gamma-1}\right)_j^{n}\left(\widehat{u}_{j+\frac{1}{2}}-\widehat{u}_{j-\frac{1}{2}}\right) \tag{5}$$

$$\left(\frac{\gamma p_\infty}{\gamma-1}\right)_j^{n+1}=\left(\frac{\gamma p_\infty}{\gamma-1}\right)_j^{n}-\frac{\Delta t}{\Delta x}\left(F^{(5)}_{j+\frac{1}{2}}-F^{(5)}_{j-\frac{1}{2}}\right)+\frac{\Delta t}{\Delta x}\left(\frac{\gamma p_\infty}{\gamma-1}\right)_j^{n}\left(\widehat{u}_{j+\frac{1}{2}}-\widehat{u}_{j-\frac{1}{2}}\right) \tag{6}$$

The single-fluid preservation criterion is stated as follows. $\left(\frac{1}{\gamma-1}\right)_j^n$ and $\left(\frac{\gamma p_\infty}{\gamma-1}\right)_j^n$ are the same for all cells if a single fluid is considered, then the updated value of $\left(\frac{1}{\gamma-1}\right)_j^{n+1}$ or $\left(\frac{\gamma p_\infty}{\gamma-1}\right)_j^{n+1}$ should not change because the physical parameter γ and p_∞ is considered as constant for a stiffened gas in a single fluid. It is easily proved that if the criterion is satisfied for the value $\left(\frac{1}{\gamma-1}\right)$, then the value $\left(\frac{\gamma p_\infty}{\gamma-1}\right)$is automatically satisfied. We therefore use only Eq. (5) to find the cell boundary velocity $\widehat{u}_{j+\frac{1}{2}}$ using the single-fluid preservation criterion.

3.1. *Lax–Friedrichs solver*

The Lax–Friedrichs (LxF) solver [21,34] is an easily implemented approximate Riemann solver and is expressed in Eq. (7).

$$\mathbf{F}_{j+\frac{1}{2}}=\frac{1}{2}\left[\mathbf{F}\left(\mathbf{U}^L_{j+\frac{1}{2}}\right)+\mathbf{F}\left(\mathbf{U}^R_{j+\frac{1}{2}}\right)\right]-\frac{1}{2}\alpha_{j+\frac{1}{2}}\left(\mathbf{U}^R_{j+\frac{1}{2}}-\mathbf{U}^L_{j+\frac{1}{2}}\right) \tag{7}$$

Here, $\alpha_{j+\frac{1}{2}}$ is the local maximum wave speed, $\alpha_{j+\frac{1}{2}}=\max\left|\lambda\left(\frac{\partial\mathbf{F}}{\partial\mathbf{U}}\right)_{j+\frac{1}{2}}\right|$, where $\lambda\left(\frac{\partial\mathbf{F}}{\partial\mathbf{U}}\right)_{j+\frac{1}{2}}$ denotes eigenvalues of the matrix $\left(\frac{\partial\mathbf{F}}{\partial\mathbf{U}}\right)_{j+\frac{1}{2}}$, where these wave speeds could be found in Appendix A.

By substituting the fourth equation of Eq. (7) into Eq. (5), we have Eq. (8).

$$\begin{aligned}\left(\frac{1}{\gamma-1}\right)_j^{n+1}&=\left(\frac{1}{\gamma-1}\right)_j^{n}\\&-\frac{\Delta t}{\Delta x}\left(\frac{1}{\gamma-1}\right)_j^{n}\left(\frac{1}{2}\left(u^L_{j+\frac{1}{2}}+u^R_{j+\frac{1}{2}}\right)-\frac{1}{2}\left(u^L_{j-\frac{1}{2}}+u^R_{j-\frac{1}{2}}\right)\right)\\&+\frac{\Delta t}{\Delta x}\left(\frac{1}{\gamma-1}\right)_j^{n}\left(\widehat{u}_{j+\frac{1}{2}}-\widehat{u}_{j-\frac{1}{2}}\right).\end{aligned} \tag{8}$$

From the single-fluid preservation criterion, we obtain the consistent cell boundary velocity for the LxF solver as in Eq. (9).

$$\widehat{u}_{j+\frac{1}{2}}=\frac{1}{2}\left(u^L_{j+\frac{1}{2}}+u^R_{j+\frac{1}{2}}\right). \tag{9}$$

This consistent cell boundary velocity in the FVM is different from the cell boundary velocity used by He et al. [13] for the FDM but is the same as that in the Roe solver of the five-equation model [3].

3.2. *Kurganov solver*

Kurganov proposed a stable Riemann-free solver for a hyperbolic system [19]. This solver has been widely applied to many hyperbolic problems, including gas dynamics [19], shallow water flow [20], and avalanche prediction [36,38]. The solver is termed as the Kurganov solver in this study. The mathematical expression for the Kurganov solver is given in Eq. (10).

$$\mathbf{F}_{j+\frac{1}{2}}=\frac{a^+_{j+\frac{1}{2}}\mathbf{F}\left(\mathbf{U}^L_{j+\frac{1}{2}}\right)-a^-_{j+\frac{1}{2}}\mathbf{F}\left(\mathbf{U}^R_{j+\frac{1}{2}}\right)}{a^+_{j+\frac{1}{2}}-a^-_{j+\frac{1}{2}}}+\frac{a^+_{j+\frac{1}{2}}a^-_{j+\frac{1}{2}}}{a^+_{j+\frac{1}{2}}-a^-_{j+\frac{1}{2}}}\left(\mathbf{U}^R_{j+\frac{1}{2}}-\mathbf{U}^L_{j+\frac{1}{2}}\right) \tag{10}$$

Here, $a^+_{j+\frac{1}{2}}$ and $a^-_{j+\frac{1}{2}}$ are the maximum and minimum wave speeds at the cell boundary; i.e., $a^+_{j+\frac{1}{2}}=\max\lambda\left(\frac{\partial\mathbf{F}}{\partial\mathbf{U}}\right)_{j+\frac{1}{2}}$ and $a^-_{j+\frac{1}{2}}=\min\lambda\left(\frac{\partial\mathbf{F}}{\partial\mathbf{U}}\right)_{j+\frac{1}{2}}$, where $\lambda()$ means all eigenvalues of a matrix. Noting that here the upper symbol + and - mean largest and smallest eigenvalue of the matrix $\left(\frac{\partial\mathbf{F}}{\partial\mathbf{U}}\right)_{j+\frac{1}{2}}$, which is different from the L and R symbol in the reconstructed process as shown in Fig. 2. Since we use primitive variables for reconstruction, we reformulated Eq. (1) by primitive variables and we derived the eigenvalues of the matrix $\left(\frac{\partial \mathbf{F}}{\partial \mathbf{U}}\right)_{j+\frac{1}{2}}$ based on the reformulated equation, please refer to appendix A for details.

By substituting the fourth term of Eq. (10) into Eq. (5), we have the updated value as in Eq. (11).

$$\left(\frac{1}{\gamma-1}\right)_j^{n+1}=\left(\frac{1}{\gamma-1}\right)_j^{n}-\frac{\Delta t}{\Delta x}\left(\frac{1}{\gamma-1}\right)_j^{n}\left(\frac{a^+_{j+\frac{1}{2}}u^L_{j+\frac{1}{2}}-a^-_{j+\frac{1}{2}}u^R_{j+\frac{1}{2}}}{a^+_{j+\frac{1}{2}}-a^-_{j+\frac{1}{2}}}-\frac{a^+_{j-\frac{1}{2}}u^L_{j-\frac{1}{2}}-a^-_{j+\frac{1}{2}}u^R_{j-\frac{1}{2}}}{a^+_{j-\frac{1}{2}}-a^-_{j-\frac{1}{2}}}\right)$$
$$+\frac{\Delta t}{\Delta x}\left(\frac{1}{\gamma-1}\right)_j^{n}\left(\widehat{u}_{j+\frac{1}{2}}-\widehat{u}_{j-\frac{1}{2}}\right) \tag{11}$$

From the single-fluid preservation criterion, we obtain the consistent boundary cell velocity for the Kurganov solver as in Eq. (12).

$$\widehat{u}_{j+\frac{1}{2}}=\frac{a^+_{j+\frac{1}{2}}u^L_{j+\frac{1}{2}}-a^-_{j+\frac{1}{2}}u^R_{j+\frac{1}{2}}}{a^+_{j+\frac{1}{2}}-a^-_{j+\frac{1}{2}}} \tag{12}$$

This consistent boundary cell velocity has not appeared in the literature before. If we select the maximum and minimum wave speeds as $a^+_{j+\frac{1}{2}}=-a^-_{j+\frac{1}{2}}=\max\left|\lambda\left(\frac{\partial \mathbf{F}}{\partial \mathbf{U}}_{j+\frac{1}{2}}\right)\right|$, then the consistent boundary cell velocity is the form of that in the LxF solver given in Eq. (9).

3.3. HLLC solver

The HLLC solver [34] is a stable Riemann solver frequently applied to hyperbolic problems [17,35] using the five-equation model. Eq. (13) expresses the HLLC solver for the γ-based model in a unified form.

$$\mathbf{F}_{j+\frac{1}{2}}=\frac{1+\operatorname{sgn}(s^*)}{2}\left[\mathbf{F}\left(\mathbf{U}^L_{j+\frac{1}{2}}\right)+s^-\left(\mathbf{q}^{*L}-\mathbf{q}^L\right)\right]$$
$$+\frac{1-\operatorname{sgn}(s^*)}{2}\left[\mathbf{F}\left(\mathbf{U}^R_{j+\frac{1}{2}}\right)+s^+\left(\mathbf{q}^{*R}-\mathbf{q}^R\right)\right] \tag{13}$$

Here, $\mathbf{q}^{*k}=\chi^{*k}\begin{pmatrix}\rho^k\\ \rho^k s^*\\ E^k+(s^*-u^k)\left(\rho^k s^*+\frac{p^k}{s^k-u^k}\right)\\ \left(\frac{1}{\gamma-1}\right)^k\\ \left(\frac{\gamma p_\infty}{\gamma-1}\right)^k\end{pmatrix}$, $\chi^{*k}=\frac{s^k-u^k}{s^k-s^*}$, $k=L, R$, $s^-=\min(0,s^L)$, $s^+=\max(0,s^R)$, and sgn is the sign function, where the + and – symbol mean maximum and minimum wave speeds similar to the Kurganov solver in 3.2. The left and right wave speeds estimated by Davis [6] are used in this study; i.e., $s^L=\min(u^L-c^L,u^R-c^R)$, $s^R=\min(u^L+c^L,u^R+c^R)$, and $s^*=\frac{p^R-p^L+\rho^Lu^L(s^L-u^L)-\rho^Ru^R(s^R-u^R)}{\rho^L(s^L-u^L)-\rho^R(s^R-u^R)}$, where c is the speed of sound. The parameters with a superscript index L or R are reconstructed parameters at cell boundary $j+\frac{1}{2}$.

With the above expressions for the HLLC solver, we obtain the fourth term of the numerical flux as in Eq. (14).

$$F^{(4)}_{j+\frac{1}{2}}=\frac{1+\operatorname{sgn}\left(s^*_{j+\frac{1}{2}}\right)}{2}\left[u^L_{j+\frac{1}{2}}\left(\frac{1}{\gamma-1}\right)^L_{j+\frac{1}{2}}+s^-_{j+\frac{1}{2}}\left(\chi^{*L}\left(\frac{1}{\gamma-1}\right)^L_{j+\frac{1}{2}}-\left(\frac{1}{\gamma-1}\right)^L_{j+\frac{1}{2}}\right)\right]$$
$$+\frac{1-\operatorname{sgn}\left(s^*_{j+\frac{1}{2}}\right)}{2}\left[u^R_{j+\frac{1}{2}}\left(\frac{1}{\gamma-1}\right)^R_{j+\frac{1}{2}}+s^+_{j+\frac{1}{2}}\left(\chi^{*R}\left(\frac{1}{\gamma-1}\right)^R_{j+\frac{1}{2}}-\left(\frac{1}{\gamma-1}\right)^R_{j+\frac{1}{2}}\right)\right] \tag{14}$$

Adopting the criterion of single-fluid preservation, we let $\left(\frac{1}{\gamma-1}\right)_j^n$ be a constant, and substituting Eq. (14) into Eq. (5), we obtain the consistent cell boundary velocity for the HLLC solver as shown in Eq. (15).

$$\widehat{u}_{j+\frac{1}{2}}=\frac{1+\operatorname{sgn}\left(s^*_{j+\frac{1}{2}}\right)}{2}\left[u^L_{j+\frac{1}{2}}+s^-_{j+\frac{1}{2}}\left(\chi^{*L}-1\right)\right]+\frac{1-\operatorname{sgn}\left(s^*_{j+\frac{1}{2}}\right)}{2}\left[u^R_{j+\frac{1}{2}}+s^+_{j+\frac{1}{2}}\left(\chi^{*R}-1\right)\right] \tag{15}$$

The consistent cell boundary velocity for the HLLC solver of the γ-based model is the same as that from the five-equation model [17], but never appeared for the γ-based model in the FVM. Therefore, we believe that the unified velocity divergence source term algorithm in this study would also be suitable for the five-equation model with other different Riemann solvers, although the justification is still needed.

The above mathematical induction gives three consistent cell boundary velocities for the three Riemann solvers, namely the LxF, Kurganov, and HLLC approximate Riemann solvers. It should be noticed that the discretization of the source terms is derived considering a first-order Euler time integrator in Eqs. (5) and (6), while we use a two- or three-step Runge-Kutta method for the computation as mentioned in Section 2.4, we now give a brief proof that the derived consistent boundary velocity will do for the two- or three-step Runge-Kutta time integrator.

Taking the two-step Runge-Kutta time integrator for an example, the derived consistent boundary velocity using first-order Euler time integrator satisfies

$$\left(\frac{1}{\gamma-1}\right)_j^{n+1}=\left(\frac{1}{\gamma-1}\right)_j^{n}-\frac{\Delta t}{\Delta x}\left(F^{(4),n}_{j+\frac{1}{2}}-F^{(4),n}_{j-\frac{1}{2}}\right)$$
$$+\frac{\Delta t}{\Delta x}\left(\frac{1}{\gamma-1}\right)_j^{n}\left(\widehat{u}^n_{j+\frac{1}{2}}-\widehat{u}^n_{j-\frac{1}{2}}\right) \tag{16}$$

$$\left(\frac{1}{\gamma-1}\right)_j^{n+2}=\left(\frac{1}{\gamma-1}\right)_j^{n+1}-\frac{\Delta t}{\Delta x}\left(F^{(4),n+1}_{j+\frac{1}{2}}-F^{(4),n+1}_{j-\frac{1}{2}}\right)$$
$$+\frac{\Delta t}{\Delta x}\left(\frac{1}{\gamma-1}\right)_j^{n+1}\left(\widehat{u}^{n+1}_{j+\frac{1}{2}}-\widehat{u}^{n+1}_{j-\frac{1}{2}}\right) \tag{17}$$

In the case of the single-fluid condition, we have

$$\left(\frac{1}{\gamma-1}\right)_j^{n+2}=\left(\frac{1}{\gamma-1}\right)_j^{n+1}=\left(\frac{1}{\gamma-1}\right)_j^{n} \tag{18}$$

Along with Eqs. (16) and (17), we have

$$\left(\frac{1}{\gamma-1}\right)_j^{n+1} = \left(\frac{1}{\gamma-1}\right)_j^{n} - \frac{\Delta t}{2\Delta x}\left[\left(F^{(4),n+1}_{j+\frac{1}{2}} - F^{(4),n+1}_{j-\frac{1}{2}}\right) - \frac{\Delta t}{\Delta x}\left(\frac{1}{\gamma-1}\right)_j^{n+1}\left(\widehat{u}^{n+1}_{j+\frac{1}{2}} - \widehat{u}^{n+1}_{j-\frac{1}{2}}\right) + \left(F^{(4),n}_{j+\frac{1}{2}} - F^{(4),n}_{j-\frac{1}{2}}\right) - \frac{\Delta t}{\Delta x}\left(\frac{1}{\gamma-1}\right)_j^{n}\left(\widehat{u}^{n}_{j+\frac{1}{2}} - \widehat{u}^{n}_{j-\frac{1}{2}}\right)\right] \tag{19}$$

Eq. (19) is the form of the discretization of the source terms using two-step Runge-Kutta method, so it come to the conclusion that the derived consistent boundary velocity will do for the two-step Runge-Kutta time integrator. It is easy to prove that the derived consistent boundary velocity will also do for the three-step Runge-Kutta time integrator. Additionally, it is remarked that the formulation is independent of the spatial reconstruction process. In summary, any standard reconstruction method with any Riemann solvers with the velocity divergence source term computational technique in this study could produce a consistent solver for the γ-based multi-fluid model.

4. Justification of the consistency with Abgrall's criterion

We here use the LxF solver as an example to prove that the consistent boundary cell velocity preserves the moving-material-interface property in Abgrall's criterion [1]. Justification for the other two Riemann solvers is presented in the appendix B. We suppose that there is a contact discontinuity moving rightward between cells I and $I+1$ (i.e., we have Eq. (20)) but other variables are discontinuous as in Eq. (21).

$$u_i^n = u_0 > 0, p_i^n = p_0 \tag{20}$$

$$\rho_i^n = \begin{cases} \rho_L & i < I \\ \rho_R & i \geq I \end{cases}, \gamma_i^n = \begin{cases} \gamma_L & i < I \\ \gamma_R & i \geq I \end{cases}, p_{\infty i}^n = \begin{cases} p_{\infty L} & i < I \\ p_{\infty R} & i \geq I \end{cases} \tag{21}$$

We next consider the evolution of physical variables in cell i right to the contact. We adopt a one-step time integration for the semi-discrete equation in Eq. (4) similar to that used by the five-equation models [31], and then mass conservation updates as in Eq. (22). The momentum update reads as Eq. (23).

$$\rho_i^{n+1} = \rho_i^n - \frac{\Delta t}{2\Delta x}\left[\left((\rho u)^R_{i+\frac{1}{2}} + (\rho u)^L_{i+\frac{1}{2}}\right) - \alpha_{i+\frac{1}{2}}\left(\rho^R_{i+\frac{1}{2}} - \rho^L_{i+\frac{1}{2}}\right) - \left((\rho u)^R_{i-\frac{1}{2}} + (\rho u)^L_{i-\frac{1}{2}}\right) + \alpha_{i-\frac{1}{2}}\left(\rho^R_{i-\frac{1}{2}} - \rho^L_{i-\frac{1}{2}}\right)\right] \tag{22}$$

$$(\rho u)_i^{n+1} = (\rho u)_i^n - \frac{\Delta t}{2\Delta x}\left\{\left[\left(\rho u^2+p\right)^R_{i+\frac{1}{2}} + \left(\rho u^2+p\right)^L_{i+\frac{1}{2}}\right] - \alpha_{i+\frac{1}{2}}\left[(\rho u)^R_{i+\frac{1}{2}} - (\rho u)^L_{i+\frac{1}{2}}\right] - \left[\left(\rho u^2+p\right)^R_{i-\frac{1}{2}} + \left(\rho u^2+p\right)^L_{i-\frac{1}{2}}\right] + \alpha_{i-\frac{1}{2}}\left[(\rho u)^R_{i-\frac{1}{2}} - (\rho u)^L_{i-\frac{1}{2}}\right]\right\} \tag{23}$$

The velocity and pressure are constant in all cells, and the pressure term in Eq. (23) thus cancels out. With velocities $u_i^n = u_0$ written outside in Eq. (23), we obtain $u_i^{n+1} = \frac{(\rho u)_i^{n+1}}{\rho_i^{n+1}} = u_0$, which implies that the updated velocity remains constant.

The above procedure is now adopted for the energy equation as in Eq. (24).

$$\left(\rho e + \frac{1}{2}\rho u^2\right)_i^{n+1} = \left(\rho e + \frac{1}{2}\rho u^2\right)_i^{n} - \frac{\Delta t}{2\Delta x}\left\{\left(u\left(\rho e + \frac{1}{2}\rho u^2 + p\right)\right)^R_{i+\frac{1}{2}} + \left(u\left(\rho e + \frac{1}{2}\rho u^2 + p\right)\right)^L_{i+\frac{1}{2}} - \alpha_{i+\frac{1}{2}}\left(\left(\rho e + \frac{1}{2}\rho u^2\right)^R_{i+\frac{1}{2}} - \left(\rho e + \frac{1}{2}\rho u^2\right)^L_{i+\frac{1}{2}}\right) - \left(u\left(\rho e + \frac{1}{2}\rho u^2 + p\right)\right)^R_{i-\frac{1}{2}} - \left(u\left(\rho e + \frac{1}{2}\rho u^2 + p\right)\right)^L_{i-\frac{1}{2}} + \alpha_{i-\frac{1}{2}}\left(\left(\rho e + \frac{1}{2}\rho u^2\right)^R_{i-\frac{1}{2}} - \left(\rho e + \frac{1}{2}\rho u^2\right)^L_{i-\frac{1}{2}}\right)\right\} \tag{24}$$

Owing to the constant distributions of velocities and pressure in all cells and the momentum conservation law in Eq. (23), the energy equation with internal energy in Eq. (2) substituted can be simplified as in Eq. (25).

$$\begin{aligned}\left(\frac{p+\gamma p_\infty}{\gamma-1}\right)_i^{n+1} = {} & \left(\frac{p+\gamma p_\infty}{\gamma-1}\right)_i^{n} - \frac{\Delta t}{2\Delta x}\Bigg\{\Bigg[\left(u\left(\frac{p+\gamma p_\infty}{\gamma-1}\right)\right)_{i+\frac{1}{2}}^{R} + \left(u\left(\frac{p+\gamma p_\infty}{\gamma-1}\right)\right)_{i+\frac{1}{2}}^{L}\Bigg] \\ & -\alpha_{i+\frac{1}{2}}\left[\left(\frac{p+\gamma p_\infty}{\gamma-1}\right)_{i+\frac{1}{2}}^{R} - \left(\frac{p+\gamma p_\infty}{\gamma-1}\right)_{i+\frac{1}{2}}^{L}\right] \\ & -\Bigg[\left(u\left(\frac{p+\gamma p_\infty}{\gamma-1}\right)\right)_{i+\frac{1}{2}}^{R} + \left(u\left(\frac{p+\gamma p_\infty}{\gamma-1}\right)\right)_{i+\frac{1}{2}}^{L}\Bigg] \\ & +\alpha_{i-\frac{1}{2}}\left[\left(\frac{p+\gamma p_\infty}{\gamma-1}\right)_{i-\frac{1}{2}}^{R} - \left(\frac{p+\gamma p_\infty}{\gamma-1}\right)_{i-\frac{1}{2}}^{L}\right]\Bigg\}\end{aligned} \tag{25}$$

The updates for γ and p_∞ are derived with constant velocities in all cells as in Eqs. (26) and (27).

$$\begin{aligned}\left(\frac{1}{\gamma-1}\right)_i^{n+1} = {} & \left(\frac{1}{\gamma-1}\right)_i^{n} - \frac{\Delta t}{2\Delta x}\Bigg[\left(\frac{u}{\gamma-1}\right)_{i+\frac{1}{2}}^{R} + \left(\frac{u}{\gamma-1}\right)_{i+\frac{1}{2}}^{L} - \alpha_{i+\frac{1}{2}}\left(\left(\frac{1}{\gamma-1}\right)_{i+\frac{1}{2}}^{R} - \left(\frac{1}{\gamma-1}\right)_{i+\frac{1}{2}}^{L}\right) \\ & -\left(\frac{u}{\gamma-1}\right)_{i-\frac{1}{2}}^{R} - \left(\frac{u}{\gamma-1}\right)_{i-\frac{1}{2}}^{L} + \alpha_{i-\frac{1}{2}}\left(\left(\frac{1}{\gamma-1}\right)_{i-\frac{1}{2}}^{R} - \left(\frac{1}{\gamma-1}\right)_{i-\frac{1}{2}}^{L}\right)\Bigg] \\ & +\frac{\Delta t}{\Delta x}\left(\frac{1}{\gamma-1}\right)_i^{n}\left[\widehat{u}_{i+\frac{1}{2}} - \widehat{u}_{i-\frac{1}{2}}\right]\end{aligned} \tag{26}$$

$$\begin{aligned}\left(\frac{\gamma p_\infty}{\gamma-1}\right)_i^{n+1} = {} & \left(\frac{\gamma p_\infty}{\gamma-1}\right)_i^{n} - \frac{\Delta t}{2\Delta x}\Bigg\{\Bigg[\left(u\left(\frac{\gamma p_\infty}{\gamma-1}\right)\right)_{i+\frac{1}{2}}^{R} + \left(u\left(\frac{\gamma p_\infty}{\gamma-1}\right)\right)_{i+\frac{1}{2}}^{L}\Bigg] - \alpha_{i+\frac{1}{2}}\left[\left(\frac{\gamma p_\infty}{\gamma-1}\right)_{i+\frac{1}{2}}^{R} - \left(\frac{\gamma p_\infty}{\gamma-1}\right)_{i+\frac{1}{2}}^{L}\right] \\ & -\Bigg[\left(u\left(\frac{\gamma p_\infty}{\gamma-1}\right)\right)_{i+\frac{1}{2}}^{R} + \left(u\left(\frac{\gamma p_\infty}{\gamma-1}\right)\right)_{i+\frac{1}{2}}^{L}\Bigg] \quad +\alpha_{i-\frac{1}{2}}\left[\left(\frac{\gamma p_\infty}{\gamma-1}\right)_{i-\frac{1}{2}}^{R} - \left(\frac{\gamma p_\infty}{\gamma-1}\right)_{i-\frac{1}{2}}^{L}\right]\Bigg\} \\ & +\frac{\Delta t}{\Delta x}\left(\frac{\gamma p_\infty}{\gamma-1}\right)_i^{n}\left[\widehat{u}_{i+\frac{1}{2}} - \widehat{u}_{i-\frac{1}{2}}\right]\end{aligned} \tag{27}$$

Note that in constant velocity field $\widehat{u}_{i+\frac{1}{2}} = \widehat{u}_{i-\frac{1}{2}} = u^L_{i+\frac{1}{2}} = u^R_{i+\frac{1}{2}} = u_0$, then the last term of velocity divergence integration $\widehat{u}_{i+\frac{1}{2}} - \widehat{u}_{i-\frac{1}{2}}$ is zero. Taking the difference between the expressions in Eqs. (25) with (27), we obtain the pressure update as in Eq. (28).

$$\begin{aligned}\left(\frac{p}{\gamma-1}\right)_i^{n+1} = {} & \left(\frac{p}{\gamma-1}\right)_i^{n} - \frac{\Delta t}{2\Delta x}\Bigg\{\Bigg[\left(u\left(\frac{p}{\gamma-1}\right)\right)_{i+\frac{1}{2}}^{R} + \left(u\left(\frac{p}{\gamma-1}\right)\right)_{i+\frac{1}{2}}^{L}\Bigg] - \alpha_{i+\frac{1}{2}}\left[\left(\frac{p}{\gamma-1}\right)_{i+\frac{1}{2}}^{R} - \left(\frac{p}{\gamma-1}\right)_{i+\frac{1}{2}}^{L}\right] \\ & -\Bigg[\left(u\left(\frac{p}{\gamma-1}\right)\right)_{i-\frac{1}{2}}^{R} + \left(u\left(\frac{p}{\gamma-1}\right)\right)_{i-\frac{1}{2}}^{L}\Bigg] \quad +\alpha_{i-\frac{1}{2}}\left[\left(\frac{p}{\gamma-1}\right)_{i-\frac{1}{2}}^{R} - \left(\frac{p}{\gamma-1}\right)_{i-\frac{1}{2}}^{L}\right]\Bigg\}\end{aligned} \tag{28}$$

Then, with $p_i^n = p_0$ written outside in Eq. (28), together with Eq. (26), we obtain $p_i^{n+1} = \left(\frac{p}{\gamma-1}\right)_i^{n+1} / \left(\frac{1}{\gamma-1}\right)_i^{n+1} = p_0$.

Taking the LxF solver as an example, we have justified that the present consistent algorithm derived from the single-fluid preservation criterion [13] is consistent with Abgrall's criterion that "the velocity and pressure equilibria should be maintained during time updates" [1]. The justification is similar for the other two approximate Riemann solvers. Please refer to the Appendix B for relevant justification for the HLLC and Kurganov solvers. Abgrall and his collaborators obtained the algorithm for the multi-fluid γ-based model with Abgrall's criterion [2,24] by handling the conservation part (i.e., the Euler equation) using the Godunov algorithm and separately handling the non-conservation part for the function of specific heat ratio ($1/(\gamma-1)$), for several different Riemann solvers. With our justification, we prove that Abgrall's criterion that "the velocity and pressure equilibria should be maintained during time updates" [1] is equivalent to the single-fluid preservation criterion [13] for the FVM. However, for the FDM, Abgrall's criterion does not yield consistent discretization [13]. Additionally, for multi-stage time integration, the consistent boundary velocity is implemented in every sub-step, therefore, the moving-material-interface property is also maintained in multi-stage time integration. It will also be proved numerically by both 1D and 2D cases in Section 5.

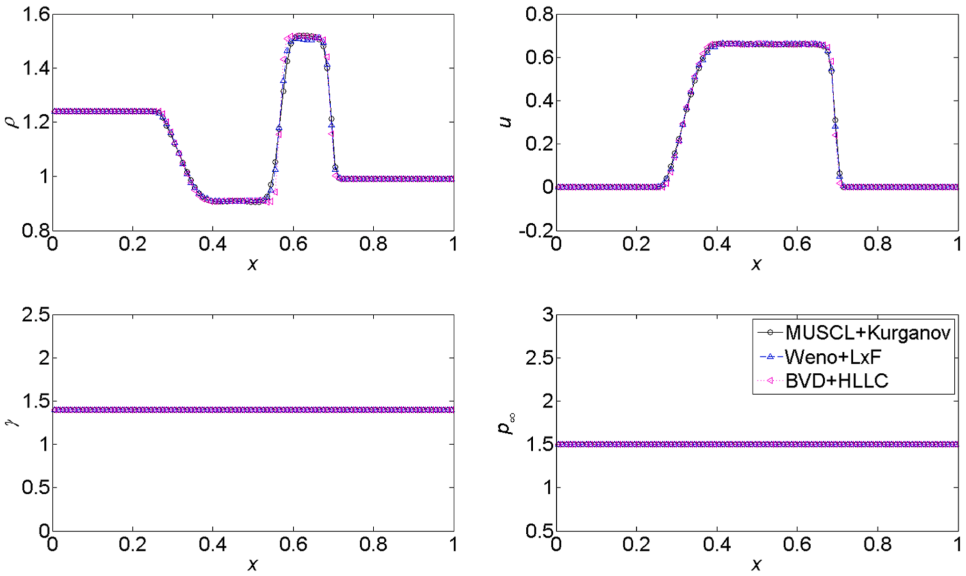

Fig. 3. Computation of the Riemann problem of a single fluid with three combinations of the reconstruction scheme and Riemann solver: (a) density, (b) velocity, (c) γ, and (d) p_∞ at dimensionless time 0.1.

5. Numerical examples and discussions

We constructed a consistent algorithm for three Riemann solvers that is independent of the reconstruction scheme. In this section, we compute several examples to numerically prove the single-fluid preservation and moving-material-interface preservation for the proposed consistent algorithms, and then other examples are presented to demonstrate the abilities of the proposed consistent algorithms.

5.1. Single-fluid preservation problem

We now have four variable reconstruction schemes, namely MUSCL, THINC, WENO, and BVD which combines two reconstruction schemes together [33], and three approximate Riemann solvers, namely LxF, Kurganov, and HLLC solvers. By combining a reconstruction scheme and Riemann solver, we have 12 numerical options in computing compressible multi-fluid flow. We use the format of the reconstruction plus Riemann solver to name a solver; e.g., MUSCL+HLLC refers to a solver with MUSCL for reconstruction and HLLC for the Riemann solver. In this subsection, we prove the single-fluid preservation numerically.

The example is a Riemann problem for liquid where the computation domain has a dimension of 1.0. The initial parameters of the problem are given in Eq. (29). All data are dimensionless. 100 cells are used, and the Courant-Friedrich-Lewy (CFL) number for time integration is 0.5.

$$\begin{pmatrix}\rho\\ u\\ p\\ \gamma\\ p_\infty\end{pmatrix}^T = \begin{cases}(1.241, 0, 2.753, 1.4, 1.504) & x < 0.5\\ (0.991, 0, 3.059E-4, 1.4, 1.504) & x > 0.5\end{cases} \tag{29}$$

Fig. 3 shows the computed results for the density, velocity, γ, and p_∞ at dimensionless time 0.1. Fig. 3(c)–(d) show that γ and p_∞ remain at their initial values, demonstrating that the single fluid is preserved by the new consistent algorithm. Fig. 3(a) reveals that the BVD reconstruction scheme sharpens the contact interface into approximately three cells, whereas the contact interface diffuses a little wider in the

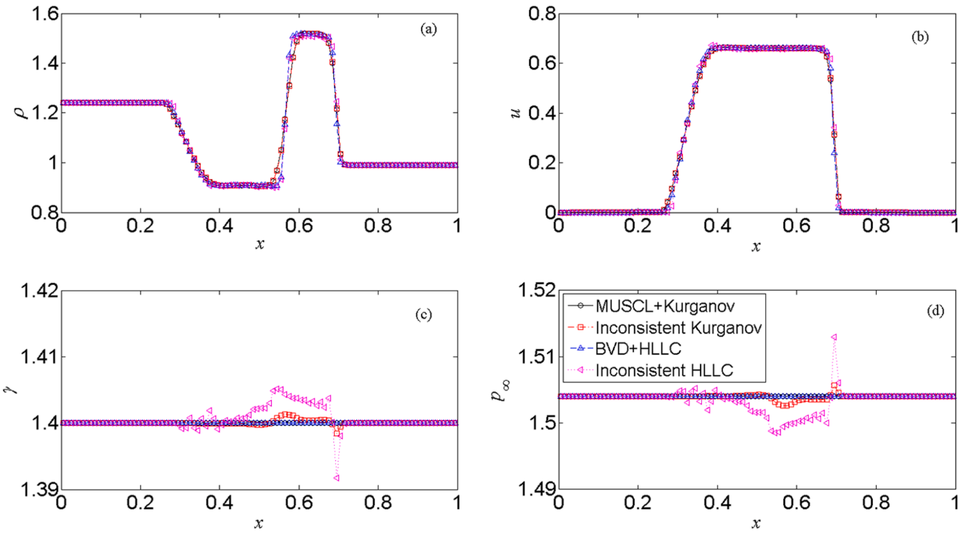

Fig. 4. Computation of the single-phase Riemann problem with two inconsistent algorithms (combining the LxF solver's cell boundary velocity in Eq. (9) instead of Eq. (12) with Kurganov and instead of Eq. (15) HLLC solvers): (a) density, (b) velocity, (c) γ, and (d) p_∞ at dimensionless time 0.1.

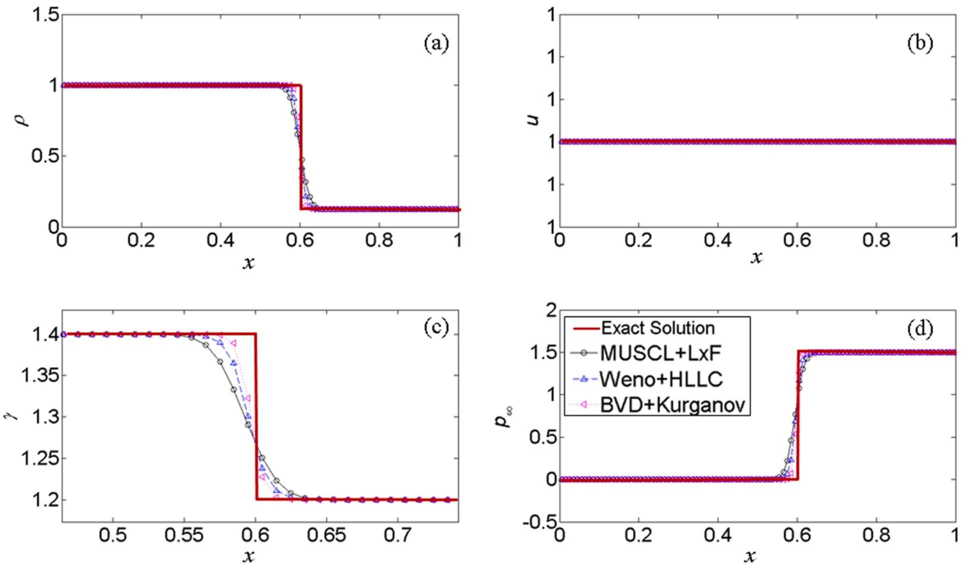

Fig. 5. Computation of the pure material interface advection problem: (a) density, (b) velocity, (c) γ, and (d) p_∞ at dimensionless time 0.1. The solid line shows the exact solution.

other reconstruction schemes.

This single-phase Riemann problem is also computed with two inconsistent algorithms combining the LxF solver's cell boundary velocity with the Kurganov solver and HLLC solver by using Eq. (9) instead of Eqs. (12) and (15). Fig. 4 presents the computational results. Fig. 4(c)–(d) show that the single-fluid property is not preserved for these two inconsistent algorithms. Errors in γ and p_∞ develop with time, resulting in errors in the computation of the pressure and sound speed.

5.2. Moving-interface problem

The compressible multi-fluid solver should preserve the pure moving-material-interface property. The initial dimensionless physical data are given in Eq. (30) for this example. In this case, a pure material phase under equilibrium should maintain a constant velocity toward the right. We use 100 cells for the calculation using three combinations of the reconstruction and Riemann solver that are different from Section 5.1. CFL number in all the cases is 0.5.

$$\begin{pmatrix} \rho \\ u \\ p \\ \gamma \\ p_\infty \end{pmatrix}^T = \begin{cases} (1.0, 1.0, 1.0, 1.4, 0) & x < 0.5 \\ (0.125, 1.0, 1.0, 1.2, 1.504) & x > 0.5 \end{cases} \tag{30}$$

Fig. 5 presents the results obtained using 100 cells for the density, velocity, γ, and p_∞ at dimensionless time 0.1. Theoretically, the material interface should move to the location of 0.6, and the computational results in Fig. 5 clearly show that the moving interface is well captured by the three methods having different combinations of the reconstruction and Riemann solver. Additionally, the velocity results presented in Fig. 5(b) show that the equilibrium condition is satisfied. The local snapshot of the interface in Fig. 5(c) implies that a BVD reconstruction results in the interface spreading by approximately 3–4 cells in this case, whereas the MUSCL reconstruction with the LxF solver predicts an interface that diffuses by 5–7 cells and the reconstruction methods of WENO predict an interface with intermediate spreading.

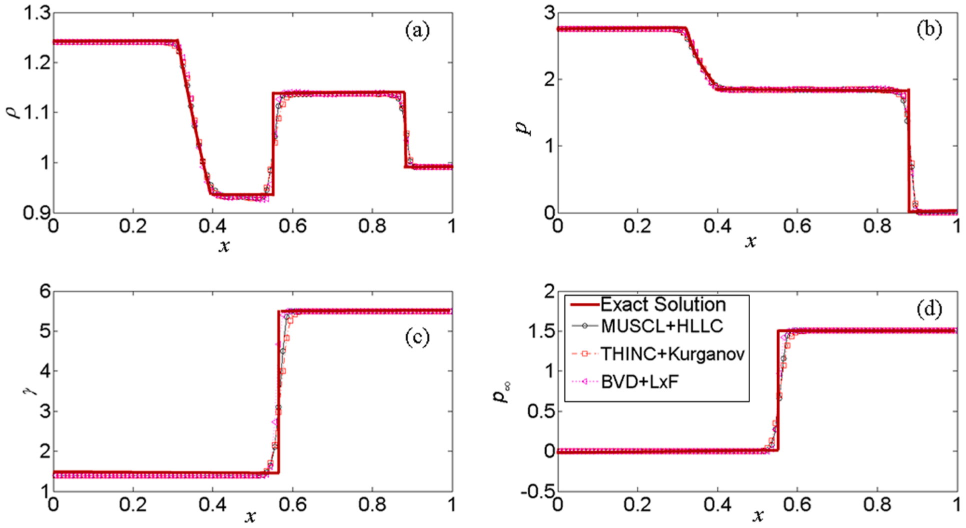

Fig. 6. Computation of the two-phase gas–liquid Riemann problem: (a) density, (b) velocity, (c) γ, and (d) p_∞ at dimensionless time 0.1. The solid line shows the exact solution [28].

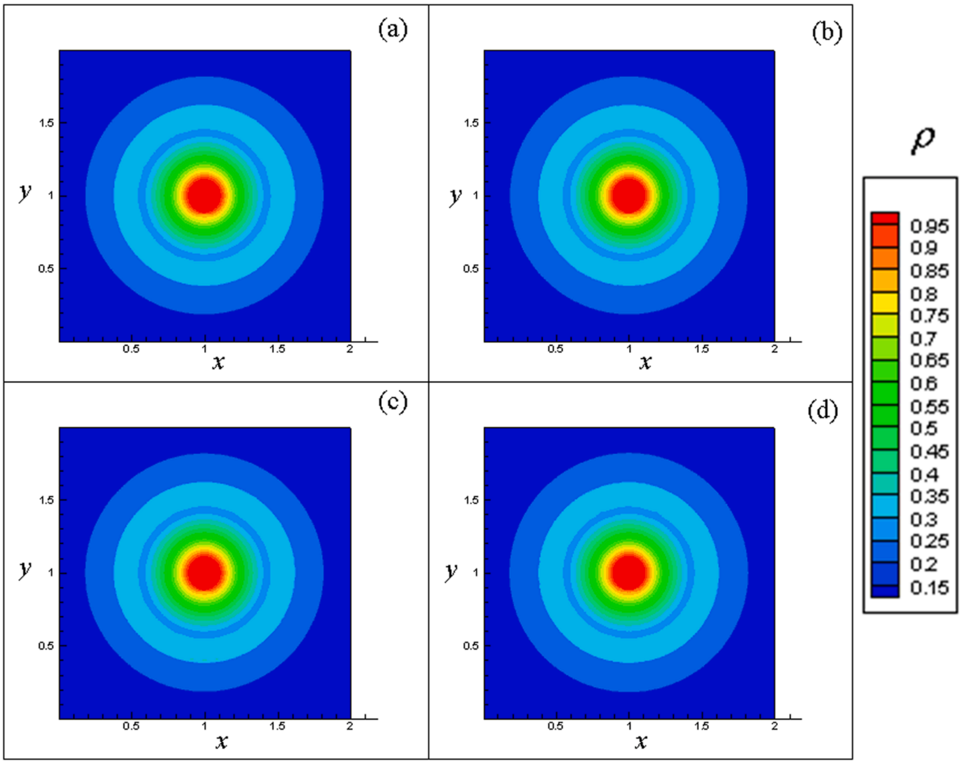

Fig. 7. Computational results of the density distribution of the 2D explosion problem in gas at dimensionless time 0.25 obtained using (a) BVD+Kurganov, (b) BVD+HLLC, (c) inconsistent Kurganov with Eq. (9) instead of Eq. (12), and (d) inconsistent HLLC solvers with Eq. (9) instead of Eq. (15).

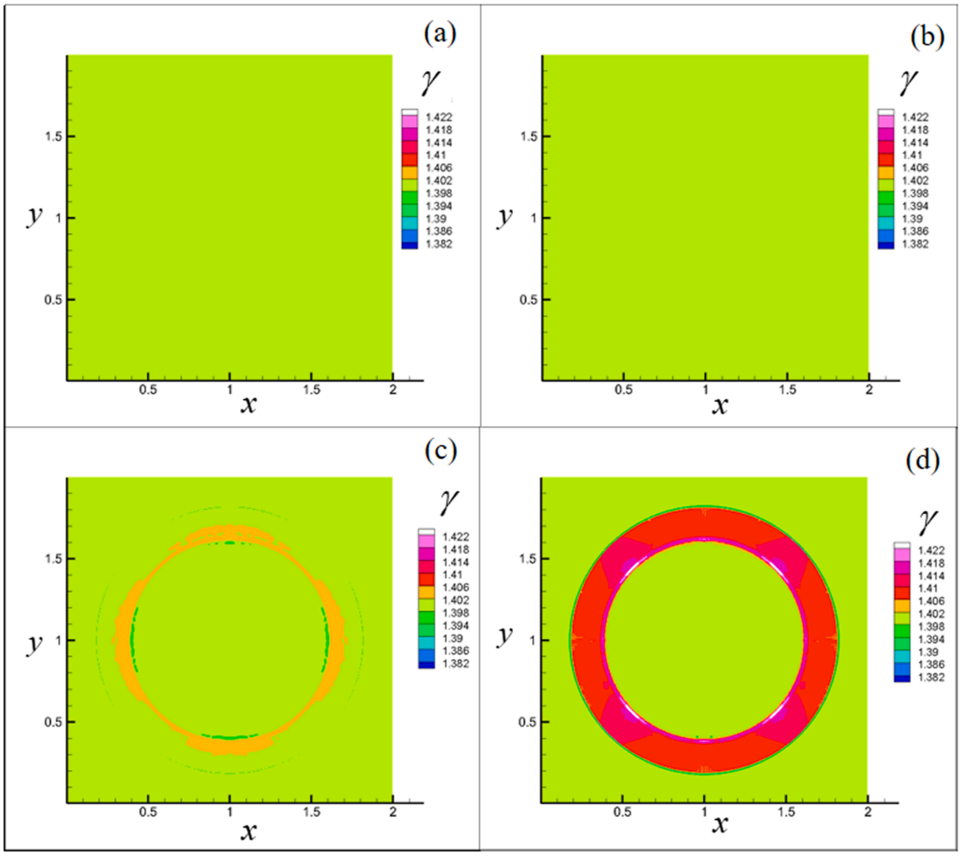

Fig. 8. Computation of the distribution of parameter γ in the two-dimensional explosion problem in gas at dimensionless time 0.25 obtained using (a) BVD+Kurganov, (b) BVD+HLLC, (C) inconsistent Kurganov with Eq. (9) instead of Eq. (12), and (d) inconsistent HLLC solvers with Eq. (9) instead of Eq. (15).

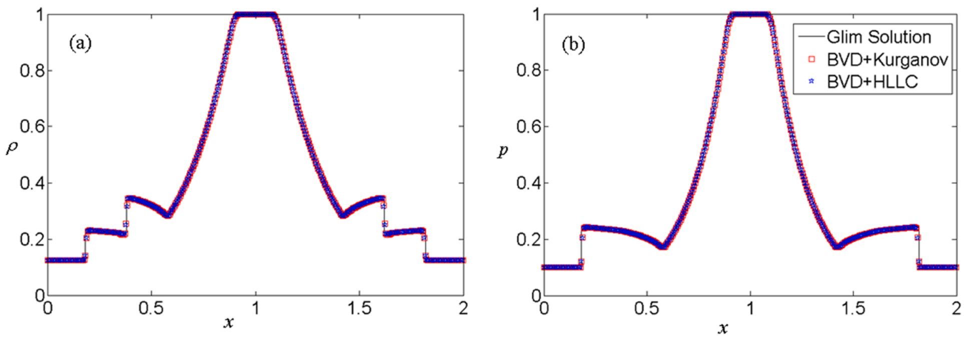

Fig. 9. Computational results of the density (a) and pressure (b) along the center line in the 2D explosion problem obtained using two solvers and their comparison with the results of Glimm's method.

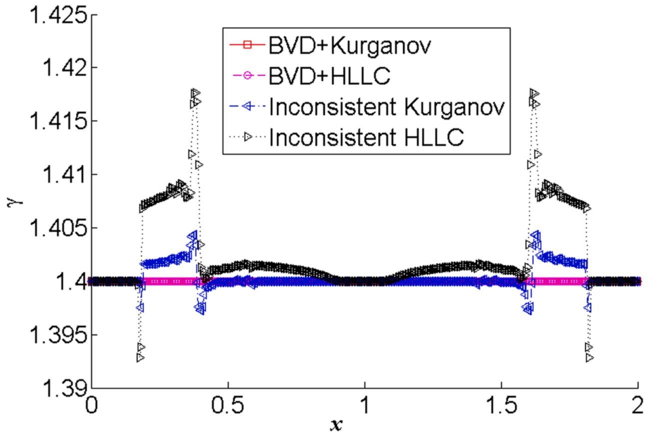

Fig. 10. Computational result of γ along the center line in the 2D explosion problem obtained using two solvers and their comparison with the results of inconsistent solvers.

5.3. *Two-phase gas–liquid Riemann problem*

The third example is the Riemann problem of a two-phase gas–liquid system. The initial physical data are given in Eq. (31).

$$\begin{pmatrix} \rho \\ u \\ p \\ \gamma \\ p_\infty \end{pmatrix}^T = \begin{cases} (1.241, 0.0, 2.753, 1.4, 0) & x < 0.5 \\ (0.991, 0.0, 3.509E-4, 5.5, 1.504) & x > 0.5 \end{cases} \tag{31}$$

Fig. 5 presents the computational results obtained using 100 cells for the density, velocity, γ, and p_∞ at dimensionless time 0.1. CFL number in all the cases is 0.5. The results agree well with the exact solutions of Shyue [28]. Both the shock front and interface are captured. The snapshots of the interface in Figs. 6(c)–(d) reveal that even with the most diffusing LxF Riemann solver, a BVD reconstruction reduces the diffusion and reduces the diffusion of the interface width to approximately 4 cells, which is narrower than the diffusion for the other three reconstruction schemes.

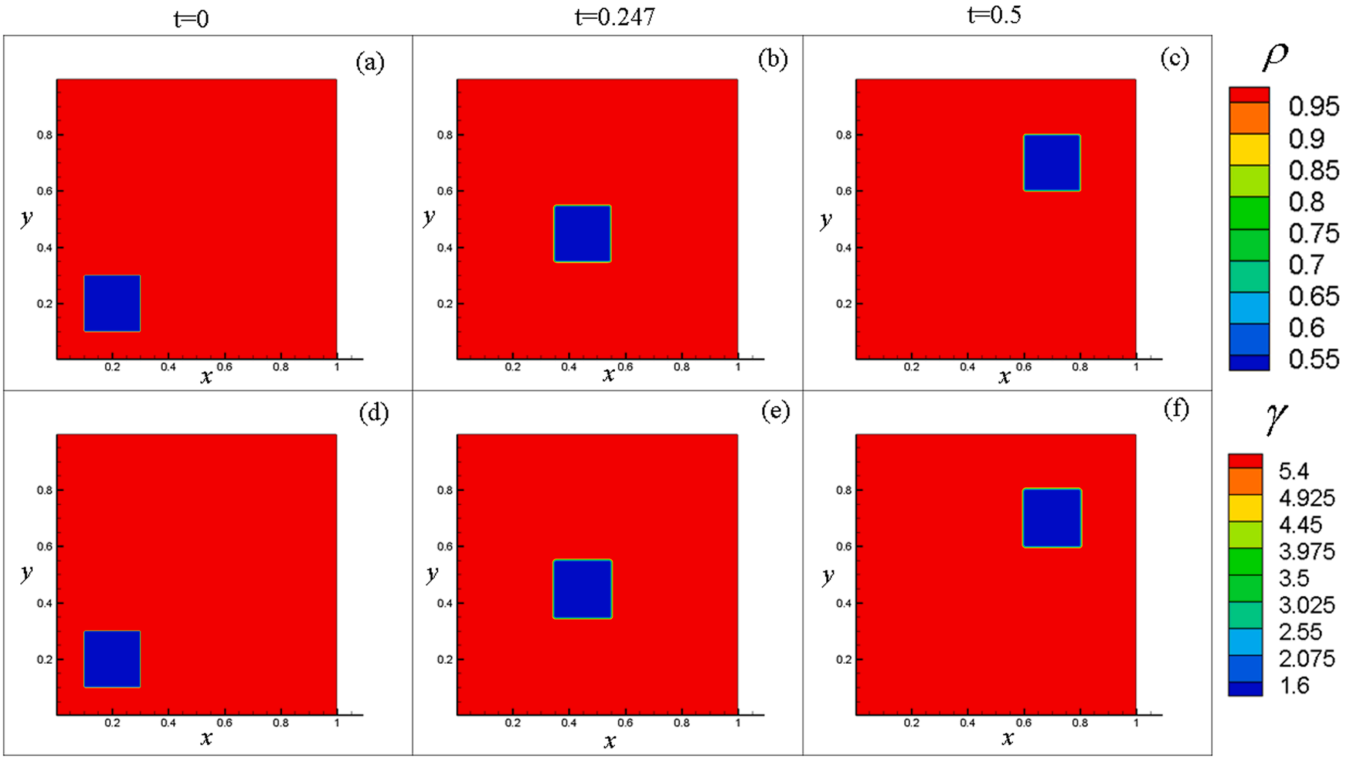

Fig. 11. Computational results of density (a–c) and γ (d–f) in the two-dimensional moving-interface problem at different times.

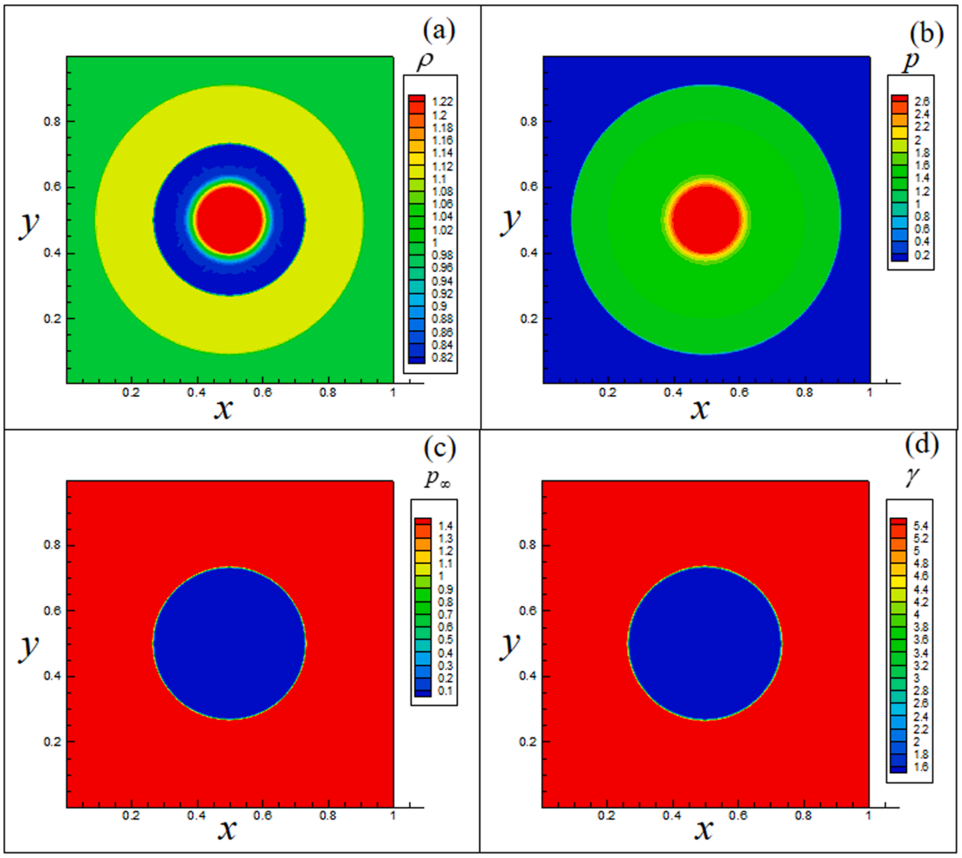

Fig. 12. Computational results of density (a), pressure (b), p_∞ (c), and γ (d) in the 2D underwater explosion problem at a dimensionless time of 0.058.

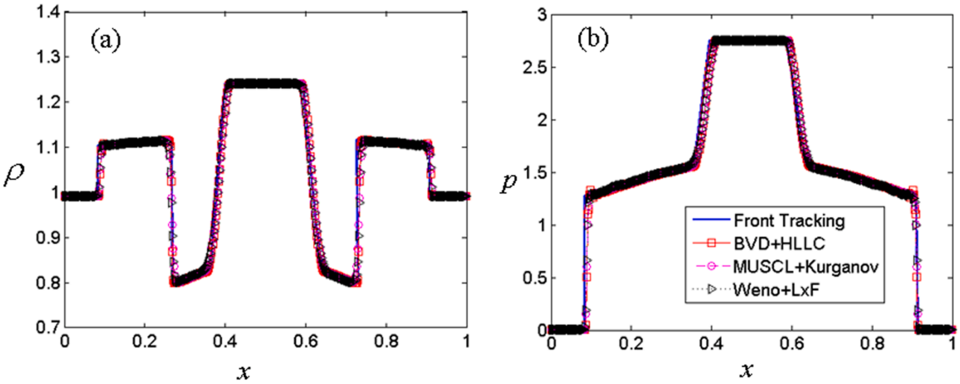

Fig. 13. Computational results of density (a) and pressure (b) along the center line obtained using different solvers and a comparison with results obtained using the front tracking method [22].

5.4. 2D single-phase explosion problem

For the 2D single-phase explosion, we simulate a classical explosion problem in gas within a domain of 2.0 × 2.0 with a high-pressure bubble at the center. The initial parameters are given in Eq. (32). We compute this problem with a 400 × 400 mesh using two solvers of BVD reconstruction combined with Kurganov and HLLC Riemann solvers. Additionally, for comparison, we present two inconsistent solvers based on the Kurganov and HLLC Riemann solvers as in Section 5.1. CFL number in all the cases is 0.5.

$$\begin{pmatrix} \rho \\ u \\ v \\ p \\ \gamma \\ p_\infty \end{pmatrix}^T = \begin{cases} (1.0, 0.0, 0.0, 1.0, 1.4, 0) & \sqrt{x^2+y^2} < 0.4 \\ (0.125, 0.0, 0.0, 0.1, 1.4, 0) & \sqrt{x^2+y^2} > 0.4 \end{cases} \tag{32}$$

Fig. 7 presents contours of the density obtained using the four solvers, where we find a circular shock moving outward with a contact discontinuity and a refraction on the inner side. Although Fig. 7(c)–(d) show density contours obtained using the two inconsistent solvers similar to those obtained by the consistent solver, Fig. 8(c)–(d) show that

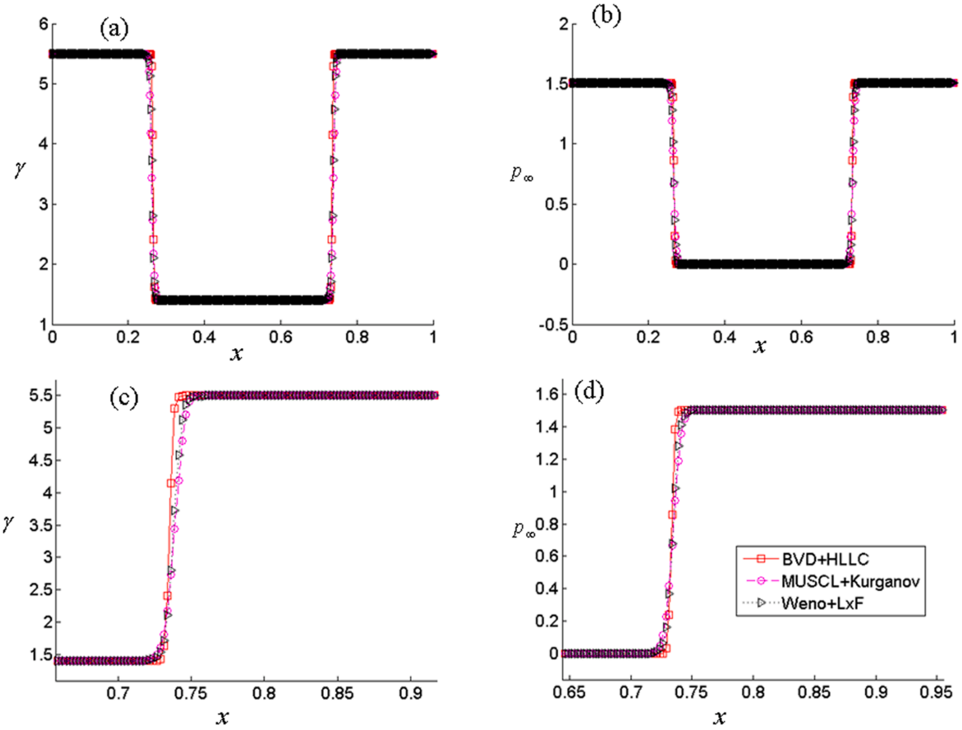

Fig. 14. Distributions of γ (a) (c) and p_∞ (b) (d) along the center line obtained using different solvers.

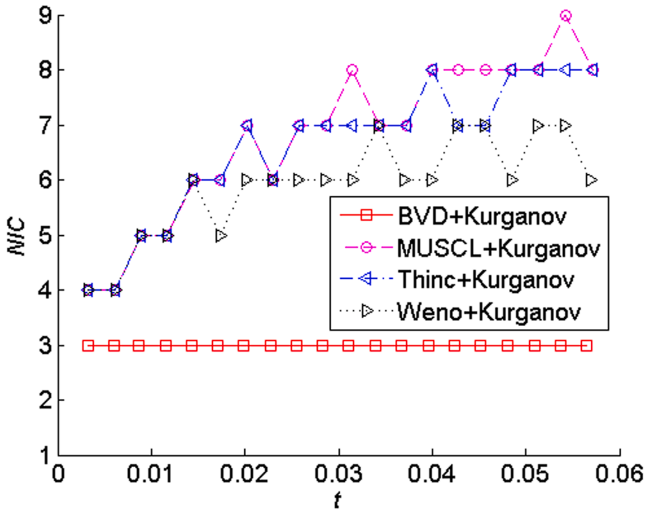

Fig. 15. Effect of the choice of reconstruction method on the computed interface width.

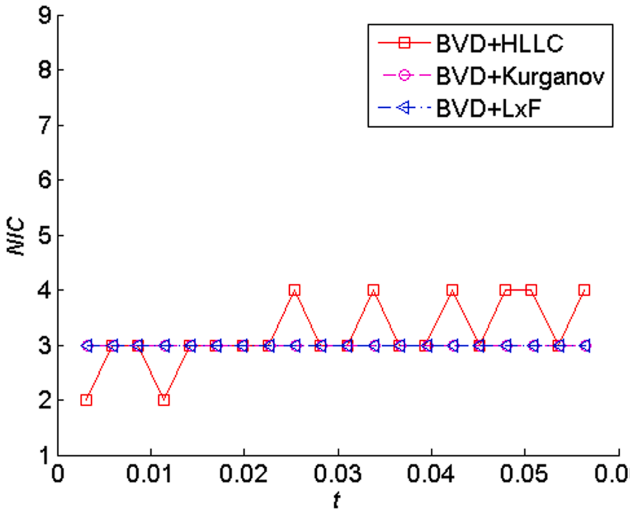

Fig. 16. Effect of the choice of Riemann solver on the computed interface width.

the single-fluid property is not preserved by these two inconsistent solvers in that error in the parameter γ diffuses greatly during the computation. Additionally, Fig. 8(a)–(b) show that the one-fluid property is preserved by the two consistent solvers.

Fig. 9 presents the distributions of density and pressure along the center line for the two consistent solvers. It is seen that the numerical solutions agree well with the computation using Glimm's random choice method [10,34]. Fig. 10 clearly shows that the two inconsistent solvers produce obvious errors in parameter γ along the center lines, whereas the two consistent solvers present the perfect single-fluid property.

5.5. 2D moving-interface problem

We simulate a square bubble traveling with a constant velocity in a liquid. The computational domain has dimensions of 1×1 and there are 300×300 cells. The initial square bubble with a side length of 0.2 lies at the position (0.2, 0.2) with a ratio of specific heats of 1.4 and density of 0.5. The surrounding environment is liquid with density of 1.0, γ of 5.5, and p_∞ of 1.504. The initial velocity throughout the field is (1,1), which means that the fluid travels from bottom-left to top-right, and the pressure is 1.0 throughout the field in equilibrium. All of the data are dimensionless. The solver combining BVD reconstruction and the Kurganov solver is used in this example. CFL number in all the cases is 0.5.

Fig. 11 presents the computational results for the contours of density

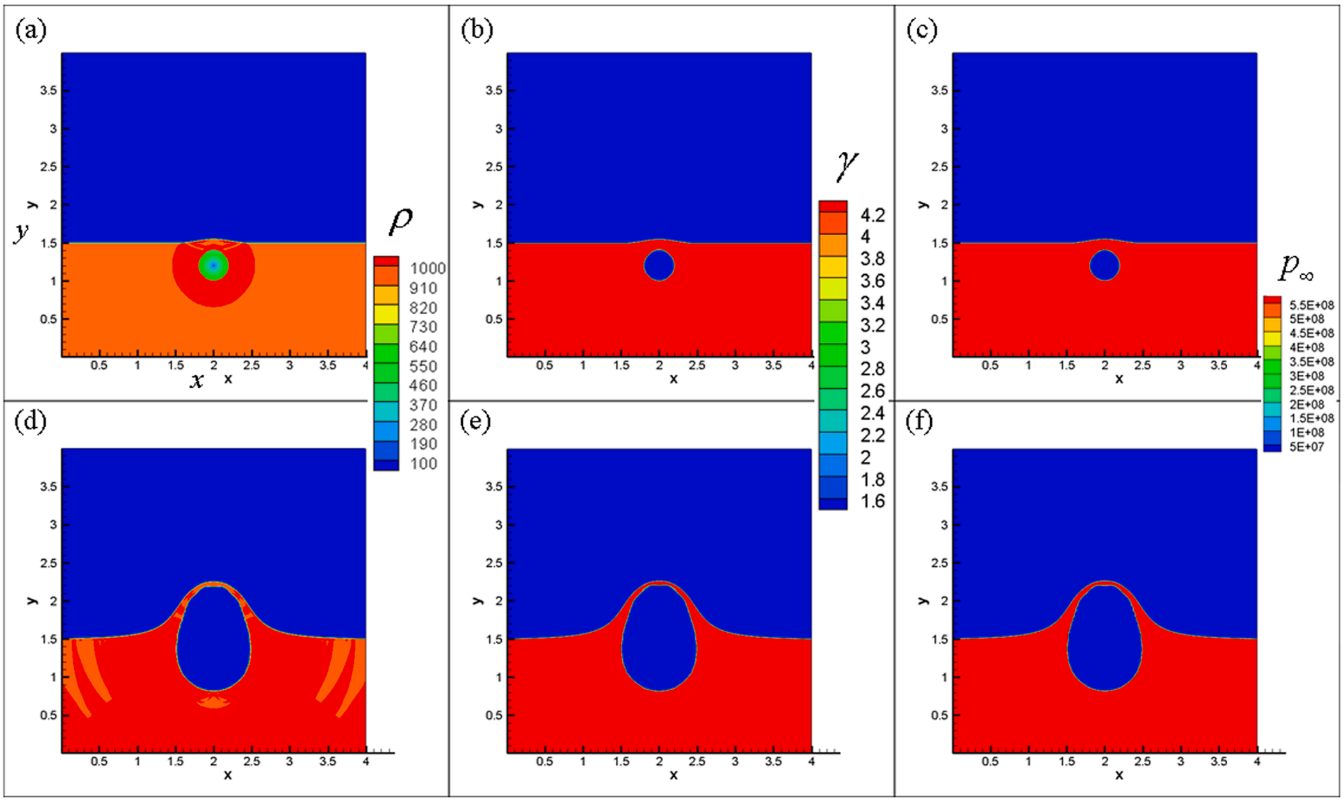

Fig. 17. Numerical results of the near-free-surface explosion: density, γ, and p_∞ at 0.2 ms (a–c) and 1.2 ms (d–f).

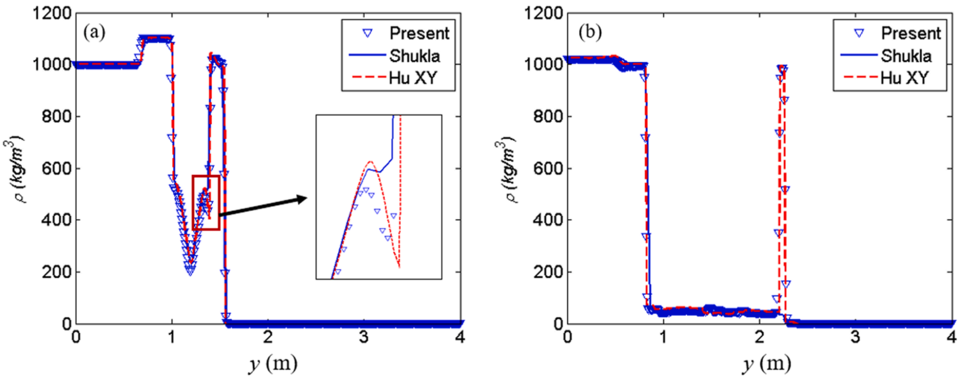

Fig. 18. Density distribution along the vertical center line (x = 2.0 m) at 0.2 and 1.2 ms for mesh resolution of 0.01 m and that obtained using the interface compression method of Shukla [27] with mesh resolution of 0.01 m and that obtained using the method of interface capture with ghost states proposed by Hu et al. [14] with mesh resolution of 0.01 m.

and γ, which agree well with the theoretical result that the bubble travels from the bottom-left corner (0.2,0.2) and reaches the top-right corner (0.7, 0.7) at dimensionless time 0.5. Additionally, it is found that the interface is constrained within a narrow width.

5.6. *Underwater explosion problem*

In this case taken from Shyue [28], we simulate a circular bubble with high internal pressure that explodes under water. The computational domain has dimensions of 1 × 1 and 400 × 400 cells are used in the simulation. Initially, a bubble with a radius of 0.2 is located at (0.5, 0.5). Within the bubble, we have $(\rho, p, \gamma, p_\infty) = (1.241, 2.753, 1.4, 0)$, whereas outside the bubble, the fluid is water with $(\rho, p, \gamma, p_\infty) = (0.991, 3.059E-4, 5.5, 1.505)$, and the velocity is zero throughout the field. All the data are dimensionless. We use several solvers with different combinations of reconstructions and Riemann solvers to simulate the problem for a duration of 0.058. CFL number in all the cases is 0.5. Fig. 12 shows results obtained using the solver that combines the BVD with the HLLC solver. After the explosion, the shock penetrates the water phase rapidly as seen in Fig. 12(b), whereas the water–air interface expands more slowly than the shock front as seen in Fig. 12(c)–(d).

Additionally, we make a quantitative comparison between the computational results obtained using our consistent solvers and the results of Shyue's front tracking method in Fig. 13. It is seen that all the combined consistent solvers with different reconstructions and Riemann solvers provide a distribution of density or pressure along the center line similar to the prediction made using the front tracking method [22].

The interface controls the physical parameters that further determine the EOS and dynamics throughout the field. We therefore plot distributions of γ and p_∞ in Fig. 14. The material interface is accurately

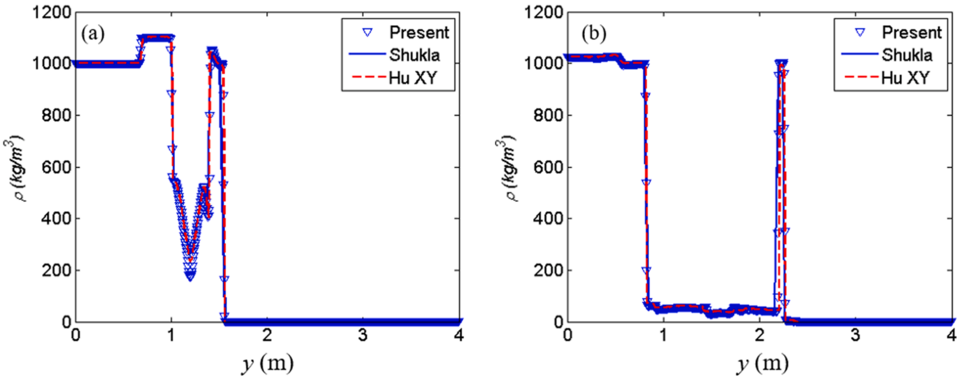

Fig. 19. Density distribution along the vertical center line ($x = 2.0$ m) at 0.2 and 1.2 ms for mesh resolution of 0.005 m and that obtained using the interface compression method of Shukla [27] with mesh resolution of 0.005 m and that obtained using the method of interface capture with ghost states proposed by Hu et al. [14] with mesh resolution of 0.01 m.

captured with different diffusion widths. The BVD+HLLC solver has the narrowest spreading of the interface width of approximately 3–4 cells, whereas the MUSCL+Kurganov solver predicts a wider interface width than the other three solvers. We therefore quantitatively assess the interface capturing ability for all the consistent solvers using the distribution of γ along the center line.

Close to a material, the parameter γ varies slowly and differs for different solvers, which increases difficulty in determining the real interface boundary. We here define an interface cell as a cell with γ between minimum and maximum values allowing 5% error. In this case, we refer to a cell with γ between 1.4 × 105% and 5.5 × 95% as an interface cell. We therefore use the number of interface cells (NIC) to characterize the interface width in assessing the interface capturing ability.

We assess the effect of the choice of reconstruction scheme and Riemann solver on the interface capturing ability. Fig. 15 shows the effect of the choice on the interface capturing ability for the same Kurganov solver. The BVD reconstruction scheme keeps the interface cell to within approximately 3 cells throughout the explosion process, whereas MUSCL diffuses the interface cell from approximately 4 to 8 or even 9 cells, the THINC reconstruction scheme has an interface capturing ability similar to that of MUSCL, and WENO appears to perform a little better than MUSCL and Thinc.

Fig. 16 presents the effect of the choice of three Riemann solvers on the interface capturing ability with BVD used for spatial reconstruction. We find that the Kurganov, and LxF have almost the same ability where the NIC remains at 3 throughout the explosion, whereas the HLLC solver presents a slight oscillation in the NIC between 2 and 4 throughout the simulation. We thus conclude that the reconstruction scheme controls the interface capturing ability more than the Riemann solvers.

5.7. *Explosion near a free surface*

We simulate an underwater explosion near a free surface, which is a problem that has been widely studied using different methods [7,14,27]. The computational region is [0,4] × [0,4] m^2 and is filled with water below 1.5 m and atmospheric air above 1.5 m as the standard state. Initially, a high-air cylinder with a radius of 0.12 m and high internal pressure (10^9 Pa) and density (1250 kg/m^3) is located at (2, 1.2) m. The specific heat ratio γ and pressure-like parameter p_∞ are, respectively 1.4 and 0.0 Pa for the air and 4.4 and 6.0×10^8 Pa for the water. The bottom wall has a reflective boundary condition and the other three boundaries an outflow boundary condition. We use the BVD+Kurganov solver to compute this problem for 3.14 ms with two meshes (400 × 400, 800 × 800), the resolutions of which are 0.01 and 0.005 m. CFL number in all the cases is 0.2. Fig. 17 presents the simulation results of density, γ and p_∞ at the two instants of 0.2 and 1.2 ms with a mesh resolution of 0.005 m.

Fig. 17 shows that the expansion of the air cylinder is well captured. The interface between the air and water is captured with high resolution. To quantitatively compare the result obtained using the present method with results obtained using other methods, we select two simulation results obtained through interface compression by Shukla [27] and interface capturing with ghost states by Hu et al. [14] Densities at the two instants obtained using the present method and the two chosen methods are compared in Fig. 18 for the mesh resolution of 0.01 m and in Fig. 19 for the mesh resolution of 0.005 m. The present consistent BVD+Kurganov solver captures the density distribution for the coarse mesh resolution of 0.01 m, and the distribution almost coincides with the result obtained through interface capturing with ghost states [14] as shown in Fig. 18. The interface compression method [27] presents far more dissipation than the present method. Fig. 19 shows that adopting a fine mesh resolution of 0.005 m in interface compression results in a density distribution having a resolution similar to that of the present method. The present method predicts a resolution of the interface similar to that of interface capturing with ghost states [14] for such complex problems with large differences in density, pressure, and parameters in the EOS.

6. Conclusions

We developed a unified consistent algorithm for the γ-based non-conservative compressible multi-fluid model with the stiffened gas equation adopted for closure. The cell boundary velocities for the integration of the source term were derived for three approximate Riemann solvers, namely the LxF, Kurganov, and HLLC solvers, which are independent of the reconstruction scheme. Several 1D and 2D examples were simulated to demonstrate that the proposed consistent algorithm preserves the one-fluid property in single-fluid flow problem and the moving-material-interface property in the two-material flow problem. The example of an underwater explosion demonstrated that sharpening reconstruction such as BVD reconstruction maintains the interface cell within approximately 3 cells for any of the above three Riemann solvers. The simulation of the near-free-surface explosion problem demonstrated that the proposed model reproduces severe compressible multi-fluid flow for an interface with large differences in density, pressure, and parameters of the EOS. The proposed consistent algorithm provides a unified framework for one kind of non-conservative hyperbolic system into a conservative hyperbolic system and a source term with velocity divergence, in which the former can be computed by a standard Godunov-type scheme and the latter can be solved using the consistent algorithm proposed in this paper. So far, the consistent algorithm is only verified for the γ-based compressible multi-fluid model, whether it could be extended to the five-equation model still needs justification both analytically and numerically.

Availability of data and material

Data can be obtained by request from the authors.

CRediT authorship contribution statement

Li Ge: Conceptualization, Methodology, Software, Validation, Formal analysis, Investigation, Writing – original draft, Writing – review & editing, Visualization. **Li Libin:** Investigation. **Liu Qingquan:** Supervision, Project administration, Funding acquisition. **Feng Chun:** Methodology, Software. **Wang Xiaoliang:** Conceptualization, Methodology, Writing – review & editing, Supervision, Project administration, Funding acquisition.

Declaration of Competing Interest

The authors declare that they have no known competing financial interests or personal relationships that could have appeared to influence the work reported in this paper.

Data availability

Data will be made available on request.

Acknowledgments

The authors acknowledge financial support from the National Natural Science Foundation of China (12172057, 12032005). We appreciate the comments by the anonymous reviewers which helps to improve the quality of this manuscript. We also thank Liwen Bianji (Edanz) (www.liwenbianji.cn) for editing the language of a draft of this manuscript.

Appendix A. Hyperbolicity of the γ-based multi-fluid model

In this appendix A, we are going prove the left part of the conservation law in Eq. (1) is a hyperbolic partial differential equation. Since we used primitive variables for reconstruction, we reformulated Eq. (1) by primitive variables as in Eq. (A-1).

$$\frac{\partial}{\partial t}\begin{pmatrix}\rho\\ u\\ p\\ \dfrac{1}{\gamma-1}\\ \dfrac{\gamma p_\infty}{\gamma-1}\end{pmatrix}+\mathbf{A}\frac{\partial}{\partial x}\begin{pmatrix}\rho\\ u\\ p\\ \dfrac{1}{\gamma-1}\\ \dfrac{\gamma p_\infty}{\gamma-1}\end{pmatrix}=\begin{pmatrix}0\\ 0\\ 0\\ \dfrac{1}{\gamma-1}\dfrac{\partial u}{\partial x}\\ \dfrac{\gamma p_\infty}{\gamma-1}\dfrac{\partial u}{\partial x}\end{pmatrix} \tag{A-1}$$

The matrix reads in Eq. (A-2).

$$\mathbf{A}=\begin{bmatrix}u & \rho & 0 & 0 & 0\\ 0 & u & \dfrac{1}{\rho} & 0 & 0\\ 0 & \gamma(p+p_\infty) & u & 0 & 0\\ 0 & \dfrac{1}{\gamma-1} & 0 & u & 0\\ 0 & \dfrac{\gamma p_\infty}{\gamma-1} & 0 & 0 & u\end{bmatrix} \tag{A-2}$$

The determinant of matrix A is derived as in Eq. (A-3), where $c=\sqrt{\frac{\gamma(p+p_\infty)}{\rho}}$ is sound speed for a stiffened gas.

$$|A-\lambda E|=(u-\lambda)^3[(\lambda-u+c)(\lambda-u-c)] \tag{A-3}$$

Then we obtained five eigenvalues of u-c, u, u, u, $u+c$ for matrix A, all of which are analytically real. Thus, we proved the original system is hyperbolic.

Appendix B. Justification of preservation of moving material interface property for Kurganov and HLLC solvers

In Section 4, we prove that the consistent boundary cell velocity derived based on the Lax–Friedrichs (LxF) solver preserves the moving-material-interface property in Abgrall's criterion [1]. In order to make our theory easier to generalize, we prove that the consistent boundary cell velocity derived based on the Kurganov and the HLLC solver preserve the moving-material-interface property in Abgrall's criterion [1] as the LxF solver. Same as demonstrated in Section 4 for LxF solver, we suppose that there is an initial contact discontinuity moving rightward between cells I and $I+1$ (i.e., we have Eq. (B-1)) but other variables are discontinuous as in Eq. (B-2).

$$u_i^n=u_0>0,p_i^n=p_0 \tag{B-1}$$

$$\rho_i^n=\begin{cases}\rho_L & i<I\\ \rho_R & i\geq I\end{cases},\gamma_i^n=\begin{cases}\gamma_L & i<I\\ \gamma_R & i\geq I\end{cases},p_{\infty i}^n=\begin{cases}p_{\infty L} & i<I\\ p_{\infty R} & i\geq I\end{cases} \tag{B-2}$$

For Kurganov solver, we consider the evolution of physical variables in cell I and the mass conservation updates as in Eq. (B-3). The momentum update reads as Eq. (B-4).

$$\begin{aligned}\rho_i^{n+1} = \rho_i^n - \frac{\Delta t}{\Delta x}\Bigg[& \frac{a_{i+\frac{1}{2}}^{+}(\rho u)_{i+\frac{1}{2}}^{L} - a_{i+\frac{1}{2}}^{-}(\rho u)_{i+\frac{1}{2}}^{R}}{a_{i+\frac{1}{2}}^{+} - a_{i+\frac{1}{2}}^{-}} + \frac{a_{i+\frac{1}{2}}^{+}a_{i+\frac{1}{2}}^{-}}{a_{i+\frac{1}{2}}^{+} - a_{i+\frac{1}{2}}^{-}}\left(\rho_{i+\frac{1}{2}}^{R} - \rho_{i+\frac{1}{2}}^{L}\right) \\ & - \frac{a_{i-\frac{1}{2}}^{+}(\rho u)_{i-\frac{1}{2}}^{L} - a_{i-\frac{1}{2}}^{-}(\rho u)_{i-\frac{1}{2}}^{R}}{a_{i-\frac{1}{2}}^{+} - a_{i-\frac{1}{2}}^{-}} - \frac{a_{i-\frac{1}{2}}^{+}a_{i-\frac{1}{2}}^{-}}{a_{i-\frac{1}{2}}^{+} - a_{i-\frac{1}{2}}^{-}}\left(\rho_{i-\frac{1}{2}}^{R} - \rho_{i-\frac{1}{2}}^{L}\right)\Bigg]\end{aligned} \tag{B-3}$$

$$\begin{aligned}(\rho u)_i^{n+1} = (\rho u)_i^n - \frac{\Delta t}{\Delta x}\Bigg[& \frac{a_{i+\frac{1}{2}}^{+}\left(\rho u^2 + p\right)_{i+\frac{1}{2}}^{L} - a_{i+\frac{1}{2}}^{-}\left(\rho u^2 + p\right)_{i+\frac{1}{2}}^{R}}{a_{i+\frac{1}{2}}^{+} - a_{i+\frac{1}{2}}^{-}} + \frac{a_{i+\frac{1}{2}}^{+}a_{i+\frac{1}{2}}^{-}}{a_{i+\frac{1}{2}}^{+} - a_{i+\frac{1}{2}}^{-}}\left((\rho u)_{i+\frac{1}{2}}^{R} - (\rho u)_{i+\frac{1}{2}}^{L}\right) \\ & - \frac{a_{i-\frac{1}{2}}^{+}\left(\rho u^2 + p\right)_{i-\frac{1}{2}}^{L} - a_{i-\frac{1}{2}}^{-}\left(\rho u^2 + p\right)_{i-\frac{1}{2}}^{R}}{a_{i-\frac{1}{2}}^{+} - a_{i-\frac{1}{2}}^{-}} - \frac{a_{i-\frac{1}{2}}^{+}a_{i-\frac{1}{2}}^{-}}{a_{i-\frac{1}{2}}^{+} - a_{i-\frac{1}{2}}^{-}}\left((\rho u)_{i-\frac{1}{2}}^{R} - (\rho u)_{i-\frac{1}{2}}^{L}\right)\Bigg]\end{aligned} \tag{B-4}$$

The velocity and pressure are constant in all cells, and the pressure term in Eq. (B-4) thus cancels out. With velocities $u_i^n = u_0$ written outside in Eq. (B-4), we obtain $u_i^{n+1} = \frac{(\rho u)_i^{n+1}}{\rho_i^{n+1}} = u_0$, which implies that the updated velocity remains constant.

The above procedure is now adopted for the energy equation as in Eq. (B-5).

$$\begin{aligned}\left(\rho e + \frac{1}{2}\rho u^2\right)_i^{n+1} = \left(\rho e + \frac{1}{2}\rho u^2\right)_i^{n} - \frac{\Delta t}{\Delta x}\Bigg[& \frac{a_{i+\frac{1}{2}}^{+}\left[u\left(\rho e + \frac{1}{2}\rho u^2 + p\right)\right]_{i+\frac{1}{2}}^{L} - a_{i+\frac{1}{2}}^{-}\left[u\left(\rho e + \frac{1}{2}\rho u^2 + p\right)\right]_{i+\frac{1}{2}}^{R}}{a_{i+\frac{1}{2}}^{+} - a_{i+\frac{1}{2}}^{-}} \\ & - \frac{a_{i-\frac{1}{2}}^{+}\left[u\left(\rho e + \frac{1}{2}\rho u^2 + p\right)\right]_{i-\frac{1}{2}}^{L} - a_{i-\frac{1}{2}}^{-}\left[u\left(\rho e + \frac{1}{2}\rho u^2 + p\right)\right]_{i-\frac{1}{2}}^{R}}{a_{i-\frac{1}{2}}^{+} - a_{i-\frac{1}{2}}^{-}} \\ & + \frac{a_{i+\frac{1}{2}}^{+}a_{i+\frac{1}{2}}^{-}}{a_{i+\frac{1}{2}}^{+} - a_{i+\frac{1}{2}}^{-}}\left(\left(\rho e + \frac{1}{2}\rho u^2\right)_{i+\frac{1}{2}}^{R} - \left(\rho e + \frac{1}{2}\rho u^2\right)_{i+\frac{1}{2}}^{L}\right) \\ & - \frac{a_{i-\frac{1}{2}}^{+}a_{i-\frac{1}{2}}^{-}}{a_{i-\frac{1}{2}}^{+} - a_{i-\frac{1}{2}}^{-}}\left(\left(\rho e + \frac{1}{2}\rho u^2\right)_{i-\frac{1}{2}}^{R} - \left(\rho e + \frac{1}{2}\rho u^2\right)_{i-\frac{1}{2}}^{L}\right)\Bigg]\end{aligned} \tag{B-5}$$

Owing to the constant distributions of velocities and pressure in all cells, and the momentum conservation law in Eq. (B-4), where in pure moving material problem, there is no energy transform by work of pressure, then the energy equation can be simplified as in Eq. (B-6).

$$\begin{aligned}\left(\frac{p + \gamma p_\infty}{\gamma - 1}\right)_i^{n+1} = \left(\frac{p + \gamma p_\infty}{\gamma - 1}\right)_i^{n} - \frac{\Delta t}{\Delta x}\Bigg\{ & \frac{a_{i+\frac{1}{2}}^{+}\left[u\frac{p + \gamma p_\infty}{\gamma - 1}\right]_{i+\frac{1}{2}}^{R} - a_{i+\frac{1}{2}}^{-}\left[u\frac{p + \gamma p_\infty}{\gamma - 1}\right]_{i+\frac{1}{2}}^{L}}{a_{i+\frac{1}{2}}^{+} - a_{i+\frac{1}{2}}^{-}} \\ & - \frac{a_{i-\frac{1}{2}}^{+}\left[u\frac{p + \gamma p_\infty}{\gamma - 1}\right]_{i-\frac{1}{2}}^{R} - a_{i-\frac{1}{2}}^{-}\left[u\frac{p + \gamma p_\infty}{\gamma - 1}\right]_{i-\frac{1}{2}}^{L}}{a_{i-\frac{1}{2}}^{+} - a_{i-\frac{1}{2}}^{-}} \\ & + \frac{a_{i+\frac{1}{2}}^{+}a_{i+\frac{1}{2}}^{-}}{a_{i+\frac{1}{2}}^{+} - a_{i+\frac{1}{2}}^{-}}\left(\left[\frac{p + \gamma p_\infty}{\gamma - 1}\right]_{i+\frac{1}{2}}^{R} - \left[\frac{p + \gamma p_\infty}{\gamma - 1}\right]_{i+\frac{1}{2}}^{L}\right) \\ & - \frac{a_{i-\frac{1}{2}}^{+}a_{i-\frac{1}{2}}^{-}}{a_{i-\frac{1}{2}}^{+} - a_{i-\frac{1}{2}}^{-}}\left(\left[\frac{p + \gamma p_\infty}{\gamma - 1}\right]_{i-\frac{1}{2}}^{R} - \left[\frac{p + \gamma p_\infty}{\gamma - 1}\right]_{i-\frac{1}{2}}^{L}\right)\Bigg\}\end{aligned} \tag{B-6}$$

The updates for γ and p_∞ are derived with constant velocities in all cells as in Eqs. (B-7) and (B-8).

$$
\begin{aligned}
\left(\frac{1}{\gamma-1}\right)_i^{n+1} = \left(\frac{1}{\gamma-1}\right)_i^{n} - \frac{\Delta t}{\Delta x}\Bigg[& \frac{a^+_{i+\frac{1}{2}}\left(u\frac{1}{\gamma-1}\right)^L_{i+\frac{1}{2}} - a^-_{i+\frac{1}{2}}\left(u\frac{1}{\gamma-1}\right)^R_{i+\frac{1}{2}}}{a^+_{i+\frac{1}{2}}-a^-_{i+\frac{1}{2}}} - \frac{a^+_{i-\frac{1}{2}}\left(u\frac{1}{\gamma-1}\right)^L_{i-\frac{1}{2}} - a^-_{i-\frac{1}{2}}\left(u\frac{1}{\gamma-1}\right)^R_{i-\frac{1}{2}}}{a^+_{i-\frac{1}{2}}-a^-_{i-\frac{1}{2}}} \\
& + \frac{a^+_{i+\frac{1}{2}}a^-_{i+\frac{1}{2}}}{a^+_{i+\frac{1}{2}}-a^-_{i+\frac{1}{2}}}\left(\left(\frac{1}{\gamma-1}\right)^R_{i+\frac{1}{2}} - \left(\frac{1}{\gamma-1}\right)^L_{i+\frac{1}{2}}\right) - \frac{a^+_{i-\frac{1}{2}}a^-_{i-\frac{1}{2}}}{a^+_{i-\frac{1}{2}}-a^-_{i-\frac{1}{2}}}\left(\left(\frac{1}{\gamma-1}\right)^R_{i-\frac{1}{2}} - \left(\frac{1}{\gamma-1}\right)^L_{i-\frac{1}{2}}\right) \\
& - \left(\frac{1}{\gamma-1}\right)^n_i\left(\frac{a^+_{i+\frac{1}{2}}u^L_{i+\frac{1}{2}} - a^-_{i+\frac{1}{2}}u^R_{i+\frac{1}{2}}}{a^+_{i+\frac{1}{2}}-a^-_{i+\frac{1}{2}}} - \frac{a^+_{i-\frac{1}{2}}u^L_{i-\frac{1}{2}} - a^-_{i-\frac{1}{2}}u^R_{i-\frac{1}{2}}}{a^+_{i-\frac{1}{2}}-a^-_{i-\frac{1}{2}}}\right)\Bigg]
\end{aligned}
\tag{B-7}
$$

$$
\begin{aligned}
\left(\frac{\gamma p_\infty}{\gamma-1}\right)_i^{n+1} = \left(\frac{\gamma p_\infty}{\gamma-1}\right)_i^{n} - \frac{\Delta t}{\Delta x}\Bigg[& \frac{a^+_{i+\frac{1}{2}}\left(u\frac{\gamma p_\infty}{\gamma-1}\right)^L_{i+\frac{1}{2}} - a^-_{i+\frac{1}{2}}\left(u\frac{\gamma p_\infty}{\gamma-1}\right)^R_{i+\frac{1}{2}}}{a^+_{i+\frac{1}{2}}-a^-_{i+\frac{1}{2}}} - \frac{a^+_{i-\frac{1}{2}}\left(u\frac{\gamma p_\infty}{\gamma-1}\right)^L_{i-\frac{1}{2}} - a^-_{i-\frac{1}{2}}\left(u\frac{\gamma p_\infty}{\gamma-1}\right)^R_{i-\frac{1}{2}}}{a^+_{i-\frac{1}{2}}-a^-_{i-\frac{1}{2}}} \\
& + \frac{a^+_{i+\frac{1}{2}}a^-_{i+\frac{1}{2}}}{a^+_{i+\frac{1}{2}}-a^-_{i+\frac{1}{2}}}\left(\left(\frac{\gamma p_\infty}{\gamma-1}\right)^R_{i+\frac{1}{2}} - \left(\frac{\gamma p_\infty}{\gamma-1}\right)^L_{i+\frac{1}{2}}\right) - \frac{a^+_{i-\frac{1}{2}}a^-_{i-\frac{1}{2}}}{a^+_{i-\frac{1}{2}}-a^-_{i-\frac{1}{2}}}\left(\left(\frac{\gamma p_\infty}{\gamma-1}\right)^R_{i-\frac{1}{2}} - \left(\frac{\gamma p_\infty}{\gamma-1}\right)^L_{i-\frac{1}{2}}\right) \\
& - \left(\frac{\gamma p_\infty}{\gamma-1}\right)^n_i\left(\frac{a^+_{i+\frac{1}{2}}u^L_{i+\frac{1}{2}} - a^-_{i+\frac{1}{2}}u^R_{i+\frac{1}{2}}}{a^+_{i+\frac{1}{2}}-a^-_{i+\frac{1}{2}}} - \frac{a^+_{i-\frac{1}{2}}u^L_{i-\frac{1}{2}} - a^-_{i-\frac{1}{2}}u^R_{i-\frac{1}{2}}}{a^+_{i-\frac{1}{2}}-a^-_{i-\frac{1}{2}}}\right)\Bigg]
\end{aligned}
\tag{B-8}
$$

Note that $u^L_{i+\frac{1}{2}} = u^R_{i+\frac{1}{2}} = u^L_{i-\frac{1}{2}} = u^R_{i-\frac{1}{2}} = u_0$, we have $\frac{a^+_{i+\frac{1}{2}}u^L_{i+\frac{1}{2}} - a^-_{i+\frac{1}{2}}u^R_{i+\frac{1}{2}}}{a^+_{i+\frac{1}{2}}-a^-_{i+\frac{1}{2}}} - \frac{a^+_{i-\frac{1}{2}}u^L_{i-\frac{1}{2}} - a^-_{i-\frac{1}{2}}u^R_{i-\frac{1}{2}}}{a^+_{i-\frac{1}{2}}-a^-_{i-\frac{1}{2}}} = 0$.

Taking the difference between the expressions in Eqs. (B-6) with (B-8), we obtain the pressure update as in Eq. (B-9).

$$
\begin{aligned}
\left(\frac{p}{\gamma-1}\right)_i^{n+1} = \left(\frac{p}{\gamma-1}\right)_i^{n} - \frac{\Delta t}{\Delta x}\Bigg\{ & \frac{a^+_{i+\frac{1}{2}}\left[u\frac{p}{\gamma-1}\right]^L_{i+\frac{1}{2}} - a^-_{i+\frac{1}{2}}\left[u\frac{p}{\gamma-1}\right]^R_{i+\frac{1}{2}}}{a^+_{i+\frac{1}{2}}-a^-_{i+\frac{1}{2}}} - \frac{a^+_{i-\frac{1}{2}}\left[u\frac{p}{\gamma-1}\right]^L_{i-\frac{1}{2}} - a^-_{i-\frac{1}{2}}\left[u\frac{p}{\gamma-1}\right]^R_{i-\frac{1}{2}}}{a^+_{i-\frac{1}{2}}-a^-_{i-\frac{1}{2}}} \\
& + \frac{a^+_{i+\frac{1}{2}}a^-_{i+\frac{1}{2}}}{a^+_{i+\frac{1}{2}}-a^-_{i+\frac{1}{2}}}\left(\left[\frac{p}{\gamma-1}\right]^R_{i+\frac{1}{2}} - \left[\frac{p}{\gamma-1}\right]^L_{i+\frac{1}{2}}\right) - \frac{a^+_{i-\frac{1}{2}}a^-_{i-\frac{1}{2}}}{a^+_{i-\frac{1}{2}}-a^-_{i-\frac{1}{2}}}\left(\left[\frac{p}{\gamma-1}\right]^R_{i-\frac{1}{2}} - \left[\frac{p}{\gamma-1}\right]^L_{i-\frac{1}{2}}\right)\Bigg\}
\end{aligned}
\tag{B-9}
$$

Then, with $p^n_i = p^R_{i+\frac{1}{2}} = p^L_{i+\frac{1}{2}} = p_0$ written outside in Eq. (B-9), which is divided by Eq. (B-7), we obtain $p^{n+1}_i = \left(\frac{p}{\gamma-1}\right)^{n+1}_i / \left(\frac{1}{\gamma-1}\right)^{n+1}_i = p_0$.

The proof for the HLLC solver is similar to that of Lax–Friedrichs Solver and the Kurganov solver mentioned before, here is a brief explanation. The flux takes the form in Eq. (B-10).

$$
\mathbf{F}_{i+\frac{1}{2}} = \frac{1+\mathrm{sgn}(s^*)}{2}\left[\mathbf{F}\left(\mathbf{U}^L_{i+\frac{1}{2}}\right) + s^-\left(\mathbf{q}^{*L} - \mathbf{q}^L\right)\right] + \frac{1-\mathrm{sgn}(s^*)}{2}\left[\mathbf{F}\left(\mathbf{U}^R_{i+\frac{1}{2}}\right) + s^+\left(\mathbf{q}^{*R} - \mathbf{q}^R\right)\right]
\tag{B-10}
$$

while the consistent cell boundary velocity takes the form in Eq. (B-11).

$$
\widehat{u}_{i+\frac{1}{2}} = \frac{1+\mathrm{sgn}\left(s^*_{i+\frac{1}{2}}\right)}{2}\left[u^L_{i+\frac{1}{2}} + s^-_{i+\frac{1}{2}}\left(\chi^{*L}-1\right)\right] + \frac{1-\mathrm{sgn}\left(s^*_{i+\frac{1}{2}}\right)}{2}\left[u^R_{i+\frac{1}{2}} + s^+_{i+\frac{1}{2}}\left(\chi^{*R}-1\right)\right]
\tag{B-11}
$$

Note that in the circumstance of Eqs. (B-1) and (B-2), we haves$^* = \frac{p^R - p^L + \rho^L u^L (s^L - u^L) - \rho^R u^R (s^R - u^R)}{\rho^L (s^L - u^L) - \rho^R (s^R - u^R)} = u_0$ and $\chi^{*k} = \frac{s^k - u^k}{s^k - s^*} = 1$. Setting $u_0 > 0$, we have $\mathbf{F}_{i+\frac{1}{2}} = \mathbf{F}\left(\mathbf{U}^L_{i+\frac{1}{2}}\right) + s^-\left(\mathbf{q}^{*L} - \mathbf{q}^L\right)$ and $\widehat{u}_{i+\frac{1}{2}} = u_0$. Furthermore, we get Eq. (B-12).

$$\mathbf{q}^{*L}-\mathbf{q}^{L}=\chi^{*k}\begin{pmatrix}\rho^{L}\\ \rho^{L}s^{L}\\ E^{L}+\left(s^{*}-u^{L}\right)\left(\rho^{L}s^{*}+\dfrac{p^{L}}{s^{L}-u^{L}}\right)\\ \left(\dfrac{1}{\gamma-1}\right)^{L}\\ \left(\dfrac{\gamma p_{\infty}}{\gamma-1}\right)^{L}\end{pmatrix}-\begin{pmatrix}\rho^{L}\\ \rho^{L}s^{L}\\ E^{L}\\ \left(\dfrac{1}{\gamma-1}\right)^{L}\\ \left(\dfrac{\gamma p_{\infty}}{\gamma-1}\right)^{L}\end{pmatrix}=0 \tag{B-12}$$

To sum up, we have the following numerical flux and boundary velocity which is rather easier than that for LxF and Kurganov solver.

$$\begin{aligned}&\mathbf{F}_{i+\frac{1}{2}}=\mathbf{F}\left(\mathbf{U}^{L}_{i+\frac{1}{2}}\right),u_{0}>0\\ &\widehat{u}_{i+\frac{1}{2}}=u_{0}\end{aligned} \tag{B-13}$$

By following the procedure of Lxf and HLLC Riemann solver, it is then easy to justify that $u_i^{n+1}=\frac{(\rho u)_i^{n+1}}{\rho_i^{n+1}}=u_0$, and $p_i^{n+1}=\left(\frac{p}{\gamma-1}\right)_i^{n+1}/\left(\frac{1}{\gamma-1}\right)_i^{n+1}=p_0$. Then the consistent boundary cell velocity derived based on the HLLC solver also preserves the moving-material-interface property in Abgrall's criterion [1].

References

[1] Abgrall R. How to prevent pressure oscillations in multicomponent flow calculations: a quasi conservative approach. J Comput Phys 1996;125:150–60.

[2] Abgrall R, Karni S. Computations of compressible multi-fluids. J Comput Phys 2001;169:594–623.

[3] Allaire G, Clerc S, Kokh S. A five-equation model for the simulation of interfaces between compressible fluids. J Comput Phys 2002;181:577–616.

[4] Aslam T, Bdzil J, Stewart D. Level set methods applied to modeling detonation shock dynamics. J Comput Phys 1996;126:390–409.

[5] Bare MR, Nunziato JW. A two-phase mixture theory for the deflagation-to-detonation transition (DDT) in reactive granular materials. Int J Multiph Flow 1986;12(6):861–89.

[6] Davis SF. Simplified second order Godunov-type methods. SIAM J Sci Stat Comput 1988;9:445–73.

[7] Deng X, Inaba S, Xie B, Shyue KM, Xiao F. High fidelity discontinuity-resolving reconstruction for compressible multiphase flows with moving interfaces. J Comput Phys 2018;371:945–66.

[8] Fedkiw R, Aslam T, Merriman B, Osher S. A non-oscillatory Eulerian approach to interfaces in multi-material flows (the ghost fluid method). J Comput Phys 1999; 152:457–92.

[9] Fu L, Hu XY, Adams NA. A family of high-order targeted eno schemes for compressible fluid simulations. J Comput Phys 2016;305:333–59.

[10] Glimm J. Solution in the large nonlinear hyperbolic systems of equations. Commun Pure Appl Math 1965;398:117–40.

[11] Glimm J, Grove J, Li X, Shyue K, Zeng Y, Zhang Q. Three-dimensional front tracking. SIAM J Sci Comput 1998;19:703–27.

[12] Haas JF, Sturtevant B. Interaction of weak shock waves with cylindrical and spherical gas inhomogeneities. J Fluid Mech 1987;181:41–76.

[13] He ZW, Li L, Zhang YS, Tian BL. Consistent implementation of characteristic flux-split based finite difference method for compressible multi-material gas flows. Comput Fluids 2018;168:190–200.

[14] Hu XY, Adams NA, Iaccarino G. On the HLLC Riemann solver for interface interaction in compressible multi-fluid flow. J Comput Phys 2009;228:6572–89.

[15] Jiang GS, Shu CW. Efficient implementation of weighted ENO schemes. J Comput Phys 1996;126:202–28.

[16] Jofre L, Urzay J. Transcritical diffuse-interface hydrodynamics of propellants in high-pressure combustors of chemical propulsion systems. Prog Energy Combust Sci 2021;82:100877.

[17] Johnsen E, Colonius T. Implementation of WENO schemes in compressible multicomponent flow problems. J Comput Phys 2006;219:715–32.

[18] Kapila AK, Menikoff R, Bdzil JB, Son SF, Stewart DS. Two-phase modeling of deflagation-to-detonation transition in granular materials: reduced equations. Phys Fluids 2001;13(10):3002–24.

[19] Kurganov A, Noelle S, Petrova G. Semidiscrete central-upwind schemes for hyperbolic conservation laws and Hamilton-Jacobi equations. SIAM J Sci Comput 2001;23(3):707–40.

[20] Kurganov A, Petrova G. A second-order well-balanced positivity preserving central-upwind scheme for the saint-venant system. Commun Math Sci 2007;5(1):133–60.

[21] LeVeque R. Finite volume methods for hyperbolic problems. Cambridge: Cambridge University Press; 2002.

[22] LeVeque RJ, Shyue KM. One-dimensional front tracking based on high resolution wave propagation methods. SIAM J Sci Comput 1995;16(2):348–77.

[23] Maltsev V, Skote M, Tsoutsanis P. High-order methods for diffuse-interface models in compressible multi-medium flows: a review. Phys Fluids 2022;34:021301.

[24] Saurel R, Abgrall R. A simple method for compressible multi-fluid flows. SIAM J Sci Comput 1999;21:1115–45.

[25] Saurel R, Pantano C. Diffuse-interface capturing methods for compressible two-phase flows. Annu Rev Fluid Mech 2018;50:105–30.

[26] Shukla RK, Pantano C, Freund JB. An interface capturing method for the simulation of multi-phase compressible flows. J Comput Phys 2010;229:7411–39.

[27] Shukla RK. Nonlinear preconditioning for efficient and accurate interface capturing in simulation of multicomponent compressible flows. J Comput Phys 2014;276: 508–40.

[28] Shyue K. An efficient shock-capturing algorithm for compressible multicomponent problems. J Comput Phys 1998;142:208–42.

[29] Shyue KM. A fluid-mixture type algorithm for compressible multicomponent flow with van der Waals equation of state. J Comput Phys 1999;156:43–88.

[30] Shyue KM. A fluid-mixture type algorithm for compressible multicomponent flow with Mie-Gruneisen equation of state. J Comput Phys 2001;171:678–707.

[31] Shyue KM, Xiao F. An Eulerian interface sharpening algorithm for compressible two-phase flow: the algebraic THINC approach. J Comput Phys 2014;268:326–54.

[32] So KK, Hu XY, Adams NA. Anti-diffusion interface sharpening technique for two-phase compressible flow simulations. J Comput Phys 2012;231:4304–23.

[33] Sun ZY, Inaba S, Xiao F. Boundary Variation Diminishing (BVD) reconstruction: a new approach to improve Godunov schemes. J Comput Phys 2016;322:309–25.

[34] Toro ET. Riemann solvers and numerical methods for fluid dynamics (3rd). Heidelberg: Springer; 2013.

[35] Wang B, Xiang GM, Hu XY. An incremental-stencil WENO reconstruction for simulation of compressible two-phase flows. Int J Multiph Flow 2018;104:20–31.

[36] Wang XL, Yang S, Yu WX, Yang XF, Liu QQ. Runout and deflection of granular flow past an array of obstacles on a slope. Eur J Mech/B Fluids 2022;94:37–49.

[37] Xiao F, Honma Y, Kono T. A simple algebraic interface capturing scheme using hyperbolic tangent function. Int J Numer Methods Fluids 2005;48:1023–40.

[38] Yang S, Wang XL, Liu QQ, Pan MH. Numerical simulation of fast granular flow facing obstacles on steep terrains. J Fluids Struct 2020;99:103162.